

Model Predictive Inferential Control of Neural State-Space Models for Autonomous Vehicle Motion Planning

Iman Askari, Xuemin Tu, Shen Zeng and Huazhen Fang

Abstract—Model predictive control (MPC) has proven useful in enabling safe and optimal motion planning for autonomous vehicles. In this paper, we investigate how to achieve MPC-based motion planning when a neural state-space model represents the vehicle dynamics. As the neural state-space model will lead to highly complex, nonlinear and nonconvex optimization landscapes, mainstream gradient-based MPC methods will be computationally too heavy to be a viable solution. In a departure, we propose the idea of model predictive inferential control (MPIC), which seeks to infer the best control decisions from the control objectives and constraints. Following the idea, we convert the MPC problem for motion planning into a Bayesian state estimation problem. Then, we develop a new particle filtering/smoothing approach to perform the estimation. This approach is implemented as banks of unscented Kalman filters/smoothers and offers high sampling efficiency, fast computation, and estimation accuracy. We evaluate the MPIC approach through a simulation study of autonomous driving in different scenarios, along with an exhaustive comparison with gradient-based MPC. The results show that the MPIC approach has considerable computational efficiency, regardless of complex neural network architectures, and shows the capability to solve large-scale MPC problems for neural state-space models.

Index Terms—Model predictive inferential control, model predictive control, motion planning, implicit importance sampling, neural-state-space model, particle filtering, particle smoothing.

I. INTRODUCTION

Autonomous driving is emerging as a transformational technology to reshape the future of transportation and bring tremendous advances in human mobility, traffic efficiency, and roadway safety [1]. A primary challenge to mature this technology is to make autonomous vehicles intelligent decision-makers so that they can drive through traffic skillfully at a level on par with, or better than, human drivers. A key decision-making task is motion planning, which is concerned with identifying the trajectories and maneuvers of the vehicle

I. Askari and H. Fang are with the Department of Mechanical Engineering, University of Kansas, Lawrence, KS 66045, USA (e-mail: askari@ku.edu; fang@ku.edu).

X. Tu is with the Department of Mathematics, University of Kansas, Lawrence, KS 66045, USA (e-mail: xuemin@ku.edu).

S. Zeng is with the Department of Electrical and System Engineering, Washington University in St.Louis, St.Louis, MO 63130, USA (e-mail: s.zeng@wustl.edu).

from a starting configuration to a goal configuration [2]. Motion plans must ensure safety in traffic, comply with driving customs or laws, and offer passenger comfort across different driving scenarios and traffic conditions.

Motion planning has attracted a large body of research in the past decades. Among the various methods, model predictive control (MPC) has demonstrated significant merits [2], [3]. At the heart, MPC enables model-based predictive optimization of motion plans in a receding-horizon fashion to provide important benefits. First, it can take advantage of the vehicle’s dynamic model and maneuverability in motion planning to achieve simultaneous path planning and tracking. Second, MPC’s innate capability of handling state and input constraints will allow to incorporate practical limits into the planning process. Such limitations typically stem from maneuver limits, safety requirements, and comfort demands. However, while MPC carries promises to compute safe and smooth motion plans, it involves nonlinear constrained optimization at its core. This means high computational costs and poor convergence guarantee to global optima [3]. These challenges persist despite recent progress on the frontier of MPC motion planner design and become even stronger in another dimension of growing importance—motion planning based on machine learning models.

Machine learning has risen as a remarkable way for vehicle modeling [4], [5]. Its unique strength lies in extracting models from data directly. Given abundant and informative data, such data-driven models based on neural networks or others can effectively capture and predict vehicle dynamics under different and even extreme driving scenarios, while showing robustness against uncertainty of various kinds, e.g., non-transparent dynamics. However, machine learning-based vehicle models will be non-trivial for MPC-based motion planning, because of their complex and highly nonlinear non-convex structure. While gradient-based optimization solvers have been used to deal with MPC of neural network models, they would be computationally expensive and even brittle in some cases, e.g., inaccurate initial guesses. The computation will be prohibitive if one pursues MPC for planning in the context of reinforcement learning [6].

In this paper, we develop an alternative framework to perform MPC motion planner design when neural network vehicle models are used. The framework, referred to as model predictive inferential control (MPIC), inherits the idea of op-

timal motion planning from MPC, but pivots away from using gradient-based optimization as solvers. Instead, it undertakes inference-driven decision-making in planning and attempts to estimate the optimal motion plans while using the driving requirements as evidence. This profound shift allows us to draw on the substantial work on nonlinear estimation in the literature and utilize various estimation methods to do MPC motion planning. Particularly powerful and attractive among those methods is particle filtering/smoothing. This technique exploits Monte Carlo sampling to achieve accurate estimation despite strong nonlinearities [7], [8] and thus provides leverage to treat the difficulty brought by neural networks to motion planning. Particle filtering/smoothing, in general, is computationally expensive due to the intensive sampling requirements in the face of nonlinearities. This motivates us to pursue a new way to do particle filtering/smoothing to execute the MPIC framework. Our approach, by design, will focus on less intensive but more effective sampling to accelerate computation.

To summarize at a high level, our study presents two main contributions.

- We propose the MPIC framework for autonomous vehicle motion planning. In this contribution, we first formulate a motion planner based on incremental-input MPC and show the equivalence of the MPC problem to a receding-horizon Bayesian state estimation problem. Then, we present the filter/smooth structure for the framework, which runs through time to estimate control decisions and generate motion plans.
- We develop a realization of the MPIC framework based on implicit particle filtering/smoothing. Our work builds upon the principle of implicit importance sampling, which asserts that, if one manages to find high-probability particles, only a moderate number of them are needed for estimation [9], [10]. Guided by this principle, we develop the implementation of implicit particle filtering/smoothing as banks of unscented Kalman filters/smoothers, which has significant computational efficiency and estimation accuracy. The MPIC realization, named as the MPIC-X algorithm, is validated via extensive simulations.

The rest of the paper is organized as follows. Section II gives a review of the related work. Section III provides an overview of autonomous vehicle motion planning in structured environments and shows the setup of the MPC planner. Section IV reformulates the incremental-input MPC problem as a Bayesian state estimation problem and then presents the MPIC framework. Section V develops the new implicit particle filtering/smoothing approach, which is implemented as banks of unscented Kalman filters/smoothers, to realize the MPIC framework, and Section VI, summarizes the discussion about the algorithm. Section VII offers simulation results to evaluate the proposed framework and algorithm for motion planning. Finally, concluding remarks are given in Section VIII.

II. RELATED WORK

A. Autonomous Vehicle Motion Planning

A vast literature has formed on motion planning for autonomous vehicles in the past years. While the problem presents itself in different formulations, exact solutions are mostly unavailable, and a diversity of numerical methods have thus flourished. An important category of them, sampling-based planning methods randomly sample across the vehicle configuration space to establish a reachability graph and then find trajectories or paths over the graph [2]. Rapidly-exploring random tree (RRT) is a popular sampling-based planner, which builds a tree incrementally by random sampling from the start to the goal configurations [11]. The method is efficient and provably converges to a suboptimal solution with probability one. More studies have well expanded the scope of RRT for autonomous vehicles, leading to many variants. They include kinodynamic RRT for planning under dynamic constraints [12] and closed-loop RRT to deal with closed-loop trajectory prediction [13]. RRT* incorporates the notion of optimality in the tree building process to become asymptotically optimal, though demanding more computation [14], [15]. In general, RRT-based methods are effective in searching through nonconvex, high-dimensional vehicle configuration spaces, for which a theoretical guarantee comes from their probabilistic completeness, i.e., they can find a solution with probability one if it exists. Trajectories that they generate, however, can be jerky and hence require postprocessing for smoothness. Tangentially related with RRT, another sampling-based planner is through particle filtering [16]. Particle filtering is based on sequential Monte Carlo sampling and when applied to motion planning, can sample trajectories based on the driving requirements to achieve better sampling efficiency. As another difference from RRT-based methods, this technique samples the lower-dimensional control input space rather than the vehicle configuration space.

Despite optimality (or suboptimality) in the probabilistic sense, sampling-based methods can hardly generate truly optimal motion plans in real world because of limited computation and time. Thus, numerical optimization has come as a natural choice to enable optimality-driven motion planning design. This approach can also conveniently include differential or non-holonomic constraints due to vehicle dynamics into the planning process. Some studies have pursued the optimization of trajectories or paths parameterized in certain forms as well as dynamic modification of preplanned paths [17]–[19]. Model predictive control (MPC) has found itself especially suitable for autonomous vehicles operating in dynamic environments and gained considerable interest recently [3], [20]–[24]. This is because it performs dynamic, receding-horizon, and predictive optimization of motion plans. Also, MPC planners can handle the primary concern in driving—safety—by including hard driving constraints resulting from safety or vehicle dynamics, and treat secondary concerns, e.g., passenger comfort and driving ethics, by encoding them into cost functions [25], [26]. However, MPC must solve nonlinear, nonconvex constrained optimization problems here, so it may struggle to converge to optimal solutions, or sometimes, feasible solutions even if they exist, and also face high computational costs [3]. To

improve convergence, the study in [25] develops a two-stage optimization framework, which enforces hard safety or driving constraints in the first stage and then polishes the solution for feasibility and smoothness within the safety bounds in the second stage. In [27], a constrained iterative linear quadratic regulator is developed to solve MPC efficiently for motion planning. In [28], the motion planning is decomposed into path planning and velocity planning so as to speed up the computation of MPC in implementation.

B. Optimal Control and MPC

The connections between control and estimation have been a fundamental research topic. The seminal work [29] by Rudolf Kalman in 1960s elucidates the duality between the linear-quadratic regulator and Kalman smoother for linear systems. Even though such exact duality was long considered hardly generalizable, some illuminating studies manage to formulate nonlinear stochastic optimal control and estimation problems dual to each other [30]–[32]. Optimal control computation often requires great amounts of time and memory, but the control-estimation synergy makes it possible to cast control design as explainable estimation problems which are more tractable to solve. A few studies pursue equivalent reformulations of stochastic optimal control as variational inference [33]–[35]. One can then use numerical variational inference methods based on stochastic optimization, Markov Chain Monte Carlo sampling, importance sampling, and others, to compute optimal control. In [36], stochastic optimal control is dealt with through recursive Bayesian state estimation based on belief propagation, though only an approximate relationship between the respective control and estimation problems in this case. However, for deterministic nonlinear systems, optimal control and MPC problems can find equivalent counterparts in recursive Bayesian state estimation problems [37], and particle filtering provides useful means to deal with these problems due to their power in handling nonlinearity. In our preliminary work [38], [39], we develop constraint-aware particle filtering/smoothing to perform nonlinear MPC with constraints.

The sweeping successes of machine learning has exponentially driven the study of learning-based MPC for dynamic systems [40], [41]. A vast literature has formed around a rich set of topics. We narrow the attention here to the specific subject of MPC of neural networks. Neural networks have a history of being used in data-driven modeling of dynamic systems. Such models are often called neural state-space (NSS) models, and MPC for them has garnered many applications [41]. To date, the solvers are mostly based on gradient-based optimization [42]–[47]. Gradient-based search, however, will easily lead MPC computation to get stuck in local minima, as NSS models are highly nonlinear and nonconvex. The study in [48] suggests to explicitly construct neural networks that are convex with respect to the input so as to avoid nonconvex optimization, but such input-convex neural networks would have restricted representation capacity. MPC of NSS models is an essential step in model-based reinforcement learning but faces unaffordable computation when applying gradient-based solutions to models based on deep neural networks.

In this context, a simple technique is to randomly generate many candidate control decision sequences and then pick the sequence that leads to the minimum cost after being applied to the NSS model [6], [49]. This technique, however, can hardly balance between accuracy and computation. The problem of MPC for NSS models hence still remains widely open to new solutions. On a related note, MPC for systems described by Gaussian processes has recently seen burgeoning studies, e.g., [5], [50], [51], and there arise similar challenges.

C. Highlights of Differences of the Study

The proposed study takes inspirations from many works in the literature, but distinguishes itself from existing research in different dimensions. A summary is as below.

This study and [16] both use particle filtering for autonomous vehicle motion planning. However, our work builds upon MPC to infuse optimality into motion planning and proposes a different, more efficient particle filtering/smoothing method to run the planning process.

The work in [37] performs MPC without constraints based on particle filtering. This study differs on several aspects. First, we consider incremental-input MPC along with constraints. Second, while conventional state-space models are the focus in [37], what we attempt to deal with is NSS models. Finally, the solver in [37] is bootstrap particle filtering, we show the need to use particle filtering/smoothing and develop a new particle filter/smooth faster and more accurate in estimation.

The work in [6], [49] uses random sampling in a forward-simulation manner to find out the best control decisions for MPC of an NSS model. Easy to implement as it is, this method requires to exhaustively search through the control space at the cost of computation to achieve just sufficient accuracy. By contrast, the particle filterer/smooth enables principled sequential Monte Carlo sampling to gain better accuracy and faster computation.

Some preliminary results of the study have appeared in [38], [39], which investigate MPC by particle filtering for motion planning. This paper presents two substantial changes. First, we consider incremental-input MPC of NSS models and convert it into the MPIC framework via Bayesian state estimation, which is more general and fits better with autonomous vehicle motion planning. Second, rather than using the bootstrap particle filter and reweighted particle smoother as in [38], [39], we develop a new implicit particle filter/smooth, which is structured as banks of unscented Kalman filters/smoothers, to execute the MPIC framework. The proposed method thus has greatly higher sampling and computational efficiency.

III. OVERVIEW OF MOTION PLANNING

In this section, we first introduce a vehicle model based on neural networks. Then, we focus on the formulation of the motion planning problem by presenting the autonomous driving requirements and subsequently setting up the MPC-based planning problem.

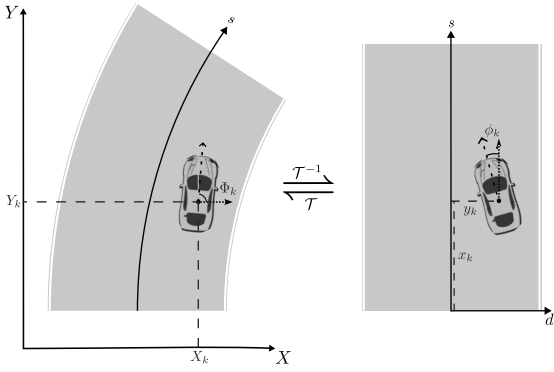


Fig. 1: Coordinate conversion between the global and Frenet coordinates.

A. Neural State-Space Vehicle Modeling

We leverage neural networks to describe the vehicle dynamics. In the global coordinate system a vehicle's state at time k is $\mathbf{X}_k = [X_k \ Y_k \ \Phi_k \ V_k]^\top$, where (X_k, Y_k) is the position, Φ_k is the heading angle, and V_k is the speed. The control input of the vehicle is $\mathbf{u}_k = [a_k \ \delta_k]^\top$, where a_k is the acceleration and δ_k is the steering angle. We consider motion planning in structured highway environments and use the Frenet coordinate frame to simplify the structure of the problem. The Frenet coordinates can be set up as follows. Suppose that a reference path is available a priori for the vehicle, which is a differentiable curve. The s -coordinate represents the longitudinal distance of the curve, and the d -coordinate represents the lateral displacement in the normal direction of the curve. The vehicle's state in the Frenet coordinates is $\mathbf{x}_k = [x_k \ y_k \ \phi_k \ V_k]^\top$, where x_k is the longitudinal position, y_k is the lateral deviation from the reference path, and ϕ_k is the yaw angle within the Frenet coordinates. One can compute the conversion between \mathbf{X}_k and \mathbf{x}_k [25]. For notational convenience, we use the transformation operator \mathcal{T} to denote the conversion:

$$\mathbf{X} = \mathcal{T}(\mathbf{x}), \quad \mathbf{x} = \mathcal{T}^{-1}(\mathbf{X}),$$

which is schematically illustrated in Fig. 1.

We use a neural network to capture the vehicle's Frenet state evolution in the continuous-time domain:

$$\dot{\mathbf{x}} = f_{\text{NN}}(\mathbf{x}, \mathbf{u}), \quad (1)$$

where $f_{\text{NN}}(\cdot)$ is a feedforward neural network. The discrete-time state evolution is then governed by

$$\mathbf{x}_{k+1} = \hat{f}(\mathbf{x}_k, \mathbf{u}_k). \quad (2)$$

We can construct \hat{f} based on (1) using different numerical discretization methods. It is often straightforward to use the finite difference method, i.e.,

$$\hat{f}(\mathbf{x}_k, \mathbf{u}_k) = \mathbf{x}_k + \Delta T \cdot f_{\text{NN}}(\mathbf{x}_k, \mathbf{u}_k),$$

which is effective if the sampling period ΔT is small enough. Alternative methods include the Runge-Kutta schemes, which are more sophisticated and offer better accuracy.

As depicted in Fig 2, the model in (2) is a recurrent neural network and also an NSS model [52]. While taking

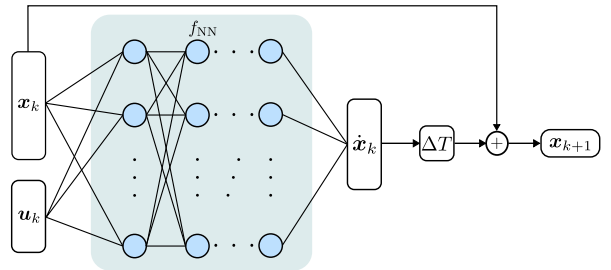


Fig. 2: Neural state-space model

a concise mathematical form, this model can use multiple hidden layers in the sense of deep learning to extract accurate representations of vehicle dynamics from data. It also admits different expansions for higher predictive accuracy. For instance, \hat{f} can be designed to use history information to do prediction [4]. In this case, its output is still \mathbf{x}_{k+1} , but its input is $\{\mathbf{x}_{k-M:k}, \mathbf{u}_{k-M:k}\}$, which is the state history over the previous M steps. However, the design in (2) suffices for our study in this paper, with the proposed results generalizable to some more complex neural network vehicle models. We will use the NSS model in (2) in the motion planning design.

Remark 1: Physics-based vehicle modeling has attracted a large amount of research in the past decades. Such models have mechanistic fidelity to a vehicle's dynamic behavior while presenting themselves in a relatively compact form as a set of nonlinear ordinary differential equations. But physical modeling often struggles to capture the full range of various uncertain effects acting on the vehicle and demands tedious human efforts in model derivation and calibration. Data-driven neural networks have thus risen in popularity for vehicle modeling in recent years. Their success results from their universal function approximation properties and powerful descriptive capabilities [4]. They also allow efficient training and deployment if abundant data are available. However, neural networks are highly nonlinear and nonconvex to require formidable amounts of computation in optimal motion planning. This is the main challenge that motivates the study in this paper.

B. Driving Requirements and Objectives

Autonomous vehicles must join traffic as responsible entities by showing safety, ethics, and predictability in their maneuver. They are hence obligated to comply with some driving requirements and constraints in motion planning and driving. Overall, the autonomous vehicle (referred to as the ego vehicle or EV) must avoid collision with other traffic participants in its vicinity (referred to as obstacle vehicles or OVs), remain within the boundaries of the road, operate in its practical actuation limits, and follow some references (in path, velocity, etc.) generated by a higher-level planning module.

Obstacle Avoidance: Collision avoidance is the top priority for motion planning. This requires the EV to always keep a safe distance from surrounding OVs. We can designate a safety area for each vehicle, which bounds it with certain margins. We denote the safety area as \mathcal{B} indiscriminately for all the EV and OVs for notational simplicity, where \mathcal{B} may take the

shape of an ellipsoid or a rectangle. At time k in the planning horizon, the EV's state is \mathbf{x}_k^{EV} , and OV i 's state is $\mathbf{x}_k^{\text{OV},i}$ for $i = 1, 2, \dots, N_O$, where N_O is the number of OVs. We then represent the areas virtually occupied by the EV and OVs, respectively, in the Frenet coordinates as

$$\mathcal{S}_k = \mathcal{S}(\mathbf{x}_k, \mathcal{B}), \quad \mathcal{O}_k^i = \mathcal{O}\left(\mathbf{x}_k^{\text{OV},i}, \mathcal{B}\right), \quad i = 1, 2, \dots, N_O.$$

Preserving safety implies

$$\mathcal{S}_k \cap \mathcal{O}_k^i = \emptyset, \quad i = 1, 2, \dots, N_O.$$

To increase the safety margin, we further impose

$$\text{dist}(\mathcal{S}_k, \mathcal{O}_k^i) \geq \underline{d}_O, \quad i = 1, 2, \dots, N_O, \quad (3)$$

where $\text{dist}(\cdot, \cdot)$ is the ordinary distance between two nonempty sets, and \underline{d}_O is the minimum distance between the EV and an OV.

Road Boundary Constraints: The EV should stay within the lane boundaries for predictable and safe driving. Its lateral deviation y_k in the Frenet coordinates then must satisfy

$$-\frac{W_L}{2} + \underline{d}_L \leq y_k \leq \frac{W_L}{2} - \underline{d}_L. \quad (4)$$

In above, W_L is the lane width, and \underline{d}_L is a restrictive margin with

$$\frac{W_{\text{EV}}}{2} < \underline{d}_L \leq \frac{W_L}{2},$$

where W_{EV} is the EV's width.

Vehicle Actuation Limits: The EV's actuation, including the acceleration and steering angle, is subject to physical limits during the maneuver. The actuation also affects the level of comfort felt by the passenger. To account for these factors, we have the following constraint in motion planning:

$$\underline{\mathbf{u}} \leq \mathbf{u}_k \leq \bar{\mathbf{u}}, \quad (5)$$

where $\underline{\mathbf{u}}$ and $\bar{\mathbf{u}}$ are the lower and upper limits, respectively. Furthermore, the EV should also bound its ramp-up and ramp-down rates in actuation to meet the need for passenger comfort and improve the smoothness in a computed motion plan. We cast this requirement as a constraint on the incremental control input $\Delta \mathbf{u}_k = \mathbf{u}_k - \mathbf{u}_{k-1}$. Specifically,

$$\Delta \underline{\mathbf{u}} \leq \Delta \mathbf{u}_k \leq \Delta \bar{\mathbf{u}}, \quad (6)$$

where $\Delta \mathbf{u}$ and $\Delta \bar{\mathbf{u}}$ are the lower and upper control increment limits, respectively.

Driving Objectives: While autonomous driving must enforce all the above constraints, it is also crucial that the EV strikes a balance between different objectives, including consistency with the prescribed reference, energy efficiency, and motion comfort, as a human driver often does. A logical approach to this end is to perform multi-objective minimization of a cost function that penalizes

- the tracking error between \mathbf{x}_k and the reference \mathbf{r}_k from the higher-level planner;
- the difference between \mathbf{u}_k and the prescribed control input reference \mathbf{s}_k ;
- the passenger discomfort resulting from \mathbf{u}_k and $\Delta \mathbf{u}_k$.

Here, \mathbf{s}_k can be selected to meet the need with tracking \mathbf{r}_k or just be zero. The case of $\mathbf{s}_k = \mathbf{0}$ implies an intention to minimize actuation efforts in driving. One may also drop this objective if they consider it insignificant in motion planning or find \mathbf{s}_k laborious to determine.

C. Motion Planning Synthesis

Having laid out the driving requirements and objectives, we are now ready to synthesize the motion planning problem. To begin with, we express the constraints in (3)-(6) notationally as

$$g_j(\mathbf{x}_k, \mathbf{u}_k, \Delta \mathbf{u}_k) \leq 0, \quad j = 1, \dots, m, \quad (7)$$

where g_j is a nonlinear or linear function depending on the specific constraint, and m is the total number of constraints. Consider motion planning within a receding horizon $[k, k+H]$, where H is the horizon length. We have the following cost function to encode the driving objectives:

$$\begin{aligned} J(\mathbf{x}_{k:k+H}, \mathbf{u}_{k:k+H}, \Delta \mathbf{u}_{k:k+H}) = \\ \sum_{t=k}^{k+H} \|\mathbf{x}_t - \mathbf{r}_t\|_{\mathbf{R}}^2 + \|\mathbf{u}_t - \mathbf{s}_t\|_{\mathbf{Q}_u}^2 + \|\Delta \mathbf{u}_t\|_{\mathbf{Q}_{\Delta u}}^2, \end{aligned}$$

where $\mathbf{x}_{k:k+H} = \{\mathbf{x}_k, \dots, \mathbf{x}_{k+H}\}$ (the same notation applies to $\mathbf{u}_{k:k+H}$ and $\Delta \mathbf{u}_{k:k+H}$), $\|\cdot\|_{\mathbf{S}}^2 = (\cdot)^\top \mathbf{S}^{-1}(\cdot)$, and \mathbf{R} , \mathbf{Q}_u and $\mathbf{Q}_{\Delta u} > 0$ are symmetric positive-definite weighting matrices. Summarizing the above, an incremental MPC problem is stated as follows for motion planning by the EV:

$$\min \quad J(\mathbf{x}_{k:k+H}, \mathbf{u}_{k:k+H}, \Delta \mathbf{u}_{k:k+H}), \quad (8a)$$

$$\text{s.t.} \quad \mathbf{x}_{t+1} = \hat{f}(\mathbf{x}_t, \mathbf{u}_t), \quad (8b)$$

$$\mathbf{u}_{t+1} = \mathbf{u}_t + \Delta \mathbf{u}_{t+1}, \quad (8c)$$

$$g_j(\mathbf{x}_t, \mathbf{u}_t, \Delta \mathbf{u}_t) \leq 0, \quad j = 1, \dots, m, \quad (8d)$$

$$t = k, \dots, k+H.$$

Based on (8), we get an online motion planner. At every time k , it computes the optimal values $\mathbf{x}_{k:k+H}^*$ and $\mathbf{u}_{k:k+H}^*$ as the current motion plan, and then repeats the procedure in a receding-horizon manner as time goes by.

Conventionally, the primary approach to solving the problem in (8) is through gradient-based numerical optimization. However, the NSS model that appears as a constraint in (8b) turns the optimization problem into a highly nonlinear and nonconvex one, thus posing an immense challenge for computation and practical implementation. Also, most numerical optimization approaches will result in only local sub-optimal solutions here—although some optimization schemes may help find global optima, they will just make the computation even more expensive [53]. Breaking away from the tradition, we will examine the above MPC problem from an estimation perspective and formulate the MPIC framework to address it.

IV. MODEL PREDICTIVE INFERRENTIAL CONTROL

In this section, we will develop the MPIC framework to control NSS models. Key to the development is recasting the MPC problem in (8) as a Bayesian state estimation problem. The resultant MPIC formulation will seek to infer or estimate,

rather than optimize as in (8), the best control decisions (i.e., motion plans) using the references and constraints (i.e., driving objectives and requirements). With this characteristic, MPIC will lend itself to be implemented by very efficient sampling-based estimation methods, as will be detailed in Section V.

A. MPC Through the Lens of State Estimation

While (8) poses a control problem, we can look at it from an estimation perspective and translate it into a Bayesian state estimation problem. The central idea lies in treating the reference and constraints as the evidence and then using the evidence to identify what the decision variables should be. To explain the idea, we begin with setting up a virtual dynamic system:

$$\begin{cases} \mathbf{x}_{t+1} = \hat{f}(\mathbf{x}_t, \mathbf{u}_t), \\ \mathbf{u}_{t+1} = \mathbf{u}_t + \Delta \mathbf{u}_{t+1}, \\ \Delta \mathbf{u}_{t+1} = \mathbf{w}_t, \\ \mathbf{y}_{\mathbf{x},t} = \mathbf{x}_t + \mathbf{v}_{\mathbf{x},t}, \\ \mathbf{y}_{\mathbf{u},t} = \mathbf{u}_t + \mathbf{v}_{\mathbf{u},t}, \\ \mathbf{y}_{g,t} = \sum_{j=1}^m \psi(g_j(\mathbf{x}_t, \mathbf{u}_t, \Delta \mathbf{u}_t)) + \varepsilon_t, \end{cases} \quad (9)$$

for $t = k, \dots, k+H$, where \mathbf{x}_t , \mathbf{u}_t and $\Delta \mathbf{u}_t$ are the state variables of the virtual system, $\mathbf{y}_{\mathbf{x},t}$, $\mathbf{y}_{\mathbf{u},t}$ and $\mathbf{y}_{g,t}$ are the measurement variables, and \mathbf{w}_t , $\mathbf{v}_{\mathbf{x},t}$, $\mathbf{v}_{\mathbf{u},t}$ and ε_t are the bounded disturbances. Also, $\psi(\cdot)$ is a barrier function used to measure the constraint satisfaction, which nominally is

$$\psi(x) = \begin{cases} 0, & x \leq 0, \\ \infty, & x > 0. \end{cases} \quad (10)$$

Note that the virtual system replicates the dynamics of the original system as considered in (8). Further, it introduces $\mathbf{y}_{\mathbf{x},t}$, $\mathbf{y}_{\mathbf{u},t}$ and $\mathbf{y}_{g,t}$ as the virtual observations of its own behavior—the behavior must correspond to how the MPC formulation in (8) steers the original system to behave. This implies that $\mathbf{y}_{\mathbf{x},t}$, $\mathbf{y}_{\mathbf{u},t}$ and $\mathbf{y}_{g,t}$ for $t = k, \dots, k+H$ in an abstract sense should take the following values, respectively:

- $\mathbf{y}_{\mathbf{x},t} = \mathbf{r}_t$ such that \mathbf{x}_t follows \mathbf{r}_t ;
- $\mathbf{y}_{\mathbf{u},t} = \mathbf{s}_t$ such that \mathbf{u}_t follows \mathbf{s}_t ;
- $\mathbf{y}_{g,t} = 0$ such that all the constraints are satisfied.

For (9), we can pose a moving horizon estimation (MHE) problem to estimate its state, which is given by

$$\min \sum_{t=k}^{k+H} \|\mathbf{v}_{\mathbf{x},t}\|_{\mathbf{R}}^2 + \|\mathbf{v}_{\mathbf{u},t}\|_{\mathbf{Q}_{\mathbf{u}}}^2 + \|\mathbf{w}_t\|_{\mathbf{Q}_{\Delta \mathbf{u}}}^2 + Q_{\varepsilon} \varepsilon_t^2, \quad (11a)$$

$$\text{s.t. } \mathbf{x}_{t+1} = \check{f}(\mathbf{x}_t, \mathbf{u}_t), \quad (11b)$$

$$\mathbf{u}_{t+1} = \mathbf{u}_t + \Delta \mathbf{u}_{t+1}, \quad (11c)$$

$$\Delta \mathbf{u}_{t+1} = \mathbf{w}_t, \quad (11d)$$

$$\mathbf{y}_{\mathbf{x},t} = \mathbf{x}_t + \mathbf{v}_{\mathbf{x},t}, \quad (11e)$$

$$\mathbf{y}_{\mathbf{u},t} = \mathbf{u}_t + \mathbf{v}_{\mathbf{u},t}, \quad (11f)$$

$$\mathbf{y}_{g,t} = \sum_{j=1}^m \psi(g_j(\mathbf{x}_t, \mathbf{u}_t, \Delta \mathbf{u}_t)) + \varepsilon_t, \quad (11g)$$

$$t = k, \dots, k+H, \quad (11h)$$

where $Q_{\varepsilon} > 0$. The above problem in (11) is mathematically equivalent to the MPC problem in (8). The only difference in their forms is that (11) transforms the hard constraints into a penalty term in the cost function as a soft constraint. The relationship between (8) and (11) recalls the duality between MPC and MHE, for which an interested reader is referred to [54]. By solving (11), we can obtain the optimal estimates of $\mathbf{x}_{k:k+H}^*$ and $\mathbf{u}_{k:k+H}^*$. But we would face the same computational struggle that afflicts (8) if using gradient-based optimization solvers. However, the MHE formulation suggests a viable alternative to solving the original MPC problem from an estimation perspective. This would open us to the opportunity of using Bayesian estimation to develop computationally fast solutions.

B. MPIC Based on Bayesian State Estimation

Proceeding forward, we write (9) compactly as

$$\begin{cases} \bar{\mathbf{x}}_{t+1} = \bar{f}(\bar{\mathbf{x}}_t) + \bar{\mathbf{w}}_t, \\ \bar{\mathbf{y}}_t = \bar{h}(\bar{\mathbf{x}}_t) + \bar{\mathbf{v}}_t, \end{cases} \quad (12)$$

where

$$\begin{aligned} \bar{\mathbf{x}}_t &= \begin{bmatrix} \mathbf{x}_t \\ \mathbf{u}_t \\ \Delta \mathbf{u}_t \end{bmatrix}, \quad \bar{\mathbf{y}}_t = \begin{bmatrix} \mathbf{y}_{\mathbf{x},t} \\ \mathbf{y}_{\mathbf{u},t} \\ \mathbf{y}_{g,t} \end{bmatrix}, \quad \bar{\mathbf{w}}_t = \begin{bmatrix} \mathbf{0} \\ \mathbf{w}_t \\ \mathbf{w}_t \end{bmatrix}, \quad \bar{\mathbf{v}}_t = \begin{bmatrix} \mathbf{v}_{\mathbf{x},t} \\ \mathbf{v}_{\mathbf{u},t} \\ \varepsilon_t \end{bmatrix}, \\ \bar{f}(\bar{\mathbf{x}}_t) &= \begin{bmatrix} \hat{f}(\mathbf{x}_t, \mathbf{u}_t) \\ \mathbf{u}_t \\ \mathbf{0} \end{bmatrix}, \quad \bar{h}(\bar{\mathbf{x}}_t) = \begin{bmatrix} \mathbf{x}_t \\ \mathbf{u}_t \\ \sum_{j=1}^m \psi(g_j(\mathbf{x}_t, \mathbf{u}_t, \Delta \mathbf{u}_t)) \end{bmatrix}. \end{aligned}$$

While (9) is subject to bounded disturbances, we relax (12) to be a stochastic system by letting $\bar{\mathbf{w}}_t$ and $\bar{\mathbf{v}}_t$ be random noise variables. This implies that $\bar{\mathbf{w}}_t$ and $\bar{\mathbf{v}}_t$ follow certain probability distributions, and the same holds for $\bar{\mathbf{x}}_t$ and $\bar{\mathbf{y}}_t$.

For (12), it is of our interest to conduct state estimation of $\bar{\mathbf{x}}_t$ for $t = k, \dots, k+H$ given $\bar{\mathbf{y}}_t = \bar{\mathbf{r}}_t$ with $\bar{\mathbf{r}}_t = [\mathbf{r}_t^\top \ \mathbf{s}_t^\top \ \mathbf{0}^\top]^\top$. This would boil down to considering the posterior probability density function $p(\bar{\mathbf{x}}_{k:k+H} | \bar{\mathbf{y}}_{k:k+H} = \bar{\mathbf{r}}_{k:k+H})$, which captures all the information or knowledge that $\bar{\mathbf{y}}_{k:k+H}$ contains about the unknown $\bar{\mathbf{x}}_{k:k+H}$. Then, to determine a quantitative estimate of $\bar{\mathbf{x}}_{k:k+H}$, a useful and popular approach is Bayesian maximum a posteriori (MAP) estimation:

$$\hat{\mathbf{x}}_{k:k+H}^* = \arg \max_{\bar{\mathbf{x}}_{k:k+H}} \log p(\bar{\mathbf{x}}_{k:k+H} | \bar{\mathbf{y}}_{k:k+H} = \bar{\mathbf{r}}_{k:k+H}). \quad (13)$$

We will use $p(\bar{\mathbf{x}}_{k:k+H} | \bar{\mathbf{y}}_{k:k+H})$ by dropping $\bar{\mathbf{r}}_{k:k+H}$ in the sequel for notational simplicity. The problem in (13) echoes the MHE problem in (11) in a way as shown below.

Theorem 1: Assume that $\bar{\mathbf{w}}_{k:k+H}$ and $\bar{\mathbf{v}}_{k:k+H}$ are mutually independent white Gaussian noise processes with

$$\bar{\mathbf{w}}_t \sim \mathcal{N}(\mathbf{0}, \bar{\mathbf{Q}}), \quad \bar{\mathbf{v}}_t \sim \mathcal{N}(\mathbf{0}, \bar{\mathbf{R}}),$$

where

$$\bar{\mathbf{Q}} = \begin{bmatrix} \mathbf{0} & \mathbf{0} & \mathbf{0} \\ \mathbf{0} & \mathbf{Q}_{\Delta \mathbf{u}} & \mathbf{Q}_{\Delta \mathbf{u}} \\ \mathbf{0} & \mathbf{Q}_{\Delta \mathbf{u}} & \mathbf{Q}_{\Delta \mathbf{u}} \end{bmatrix}, \quad \bar{\mathbf{R}} = \text{diag}(\mathbf{R}, \mathbf{Q}_{\mathbf{u}}, Q_{\varepsilon}).$$

Then, the problems in (11) and (13) will have the same optima.

Proof: Using Bayes' rule and the Markovian property of (9), we have

$$p(\bar{\mathbf{x}}_{k:k+H} | \bar{\mathbf{y}}_{k:k+H}) \propto \prod_{t=k}^{k+H} p(\bar{\mathbf{y}}_t | \bar{\mathbf{x}}_t) \prod_{t=k+1}^{k+H} p(\bar{\mathbf{x}}_t | \bar{\mathbf{x}}_{t-1}) p(\bar{\mathbf{x}}_k),$$

which implies

$$\begin{aligned} \log p(\bar{\mathbf{x}}_{k:k+H} | \bar{\mathbf{y}}_{k:k+H}) &= \sum_{t=k}^{k+H} \log p(\bar{\mathbf{y}}_t | \bar{\mathbf{x}}_t) \\ &+ \sum_{t=k+1}^{k+H} \log p(\bar{\mathbf{x}}_t | \bar{\mathbf{x}}_{t-1}) + \log p(\bar{\mathbf{x}}_k). \end{aligned}$$

Because $p(\bar{\mathbf{y}}_t | \bar{\mathbf{x}}_t) = p(\bar{\mathbf{v}}_t) \sim \mathcal{N}(\mathbf{0}, \bar{\mathbf{R}})$, we get

$$\log p(\bar{\mathbf{y}}_t | \bar{\mathbf{x}}_t) \propto \|\bar{\mathbf{v}}_t\|_{\bar{\mathbf{R}}}^2.$$

Further, $p(\bar{\mathbf{x}}_t | \bar{\mathbf{x}}_{t-1}) = p(\bar{\mathbf{w}}_t) \sim \mathcal{N}(\mathbf{0}, \bar{\mathbf{Q}})$. This is a degenerate Gaussian distribution since $\bar{\mathbf{Q}}$ is rank-deficient. As \mathbf{w}_t is the only random vector in $\bar{\mathbf{w}}_t$, we have $p(\bar{\mathbf{w}}_t) = p(\mathbf{w}_t)$, which can also be derived using the disintegration theorem [55, Theorem 5.4]. Then, it follows that

$$\log p(\bar{\mathbf{x}}_t | \bar{\mathbf{x}}_{t-1}) \propto \|\mathbf{w}_t\|_{Q_{\Delta u}}^2,$$

for $t = k+1, \dots, k+H$. In a similar way, $p(\bar{\mathbf{x}}_k) = p(\mathbf{w}_k)$, and $\log p(\bar{\mathbf{x}}_k) = \|\mathbf{w}_k\|_{Q_{\Delta u}}^2$. Putting together the above, we find that the cost function in (13) is given by

$$\sum_{t=k}^{k+H} \|\bar{\mathbf{v}}_t\|_{\bar{\mathbf{R}}}^2 + \|\mathbf{w}_k\|_{Q_{\Delta u}}^2,$$

which is the opposite of the cost function in (11). The theorem is thus proven. \blacksquare

Theorem 1 suggests the equivalence of the two estimation problems in a Gaussian setting, by showing that the maxima of (13) coincide with the minima of (11). This key connection allows us to focus on tackling (13) in the sequel. In general, it is not possible to find an analytical solution to (13), but we can still develop computable approaches to perform the estimation. The estimation results will make an approximate solution to (11) and, in turn, the original MPC problem in (8).

The MAP estimation problem in (13) is known as a smoothing problem in estimation theory, which refers to the reconstruction of the past states using the measurement history. For a stochastic system, this is concerned with computing $p(\bar{\mathbf{x}}_{k:k+H} | \bar{\mathbf{y}}_{k:k+H})$, and one can break down the computation into two passes [8]. The first is the forward filtering pass, which is governed by

$$p(\bar{\mathbf{x}}_{k:t} | \bar{\mathbf{y}}_{k:t}) = p(\bar{\mathbf{y}}_t | \bar{\mathbf{x}}_t) p(\bar{\mathbf{x}}_t | \bar{\mathbf{x}}_{t-1}) p(\bar{\mathbf{x}}_{k:t-1} | \bar{\mathbf{y}}_{k:t-1}), \quad (14)$$

for $t = k, \dots, k+H$. This relation shows the a recursive update from $p(\bar{\mathbf{x}}_{k:t-1} | \bar{\mathbf{y}}_{k:t-1})$ to $p(\bar{\mathbf{x}}_{k:t} | \bar{\mathbf{y}}_{k:t})$. The smoothing pass follows the completion of the filtering, which starts from $p(\bar{\mathbf{x}}_{k+H} | \bar{\mathbf{y}}_{k:k+H})$ and goes all the way back to $p(\bar{\mathbf{x}}_k | \bar{\mathbf{y}}_{k:k+H})$. This is through the backward recursion based on

$$\begin{aligned} p(\bar{\mathbf{x}}_{t:k+H} | \bar{\mathbf{y}}_{k:k+H}) &= p(\bar{\mathbf{x}}_t | \bar{\mathbf{x}}_{t+1}, \bar{\mathbf{y}}_k) \\ &\cdot p(\bar{\mathbf{x}}_{t+1:k+H} | \bar{\mathbf{y}}_{k:k+H}), \end{aligned} \quad (15)$$

Algorithm 1 The MPIC Framework

```

1: Formulate the MPC problem in (8)
2: Set up the virtual system in (9)
3: for  $k = 1, 2, \dots$  do
   // Forward filtering
4:   for  $t = k, k+1, \dots, k+H$  do
5:     Compute  $p(\bar{\mathbf{x}}_t | \bar{\mathbf{y}}_{k:t})$  via (14)
6:   end for
   // Backward smoothing
7:   for  $t = k+H-1, k+H-2, \dots, k$  do
8:     Compute  $p(\bar{\mathbf{x}}_t | \bar{\mathbf{y}}_{k:k+H})$  via (15)
9:   end for
10:  Compute  $\hat{\bar{\mathbf{x}}}_{k:k+H}^*$ , and apply control
11: end for

```

for $t = k+H-1, \dots, k$. After the smoothing, we can extract $\hat{\bar{\mathbf{x}}}_{k:k+H}^*$ and then run the two-pass procedure repeatedly at subsequent times.

Based on the above, we summarize the MPIC framework in Algorithm 1. Characteristically, the framework exploits Bayesian inference based on forward-backward smoothing to implement MPC, in a shift away from gradient-based numerical optimization. The core notion is that we can estimate the best control decisions based on the control task specifications and requirements. The perspective shift will bring considerable computational merits for control design of NSS models. First, Bayesian state estimation has a recursive processing structure as a result of using the Markovian property of a dynamic system, as is shown by (14)-(15). The structure yields sequential computation in conducting inference to lower the computational burden. Second, a main challenge in Bayesian state estimation for complex systems is how to tame both nonlinearity and computation. The rich literature on the challenge provides a source of inspirations and insights to enable computationally efficient MPIC design for NSS models. For example, sequential Monte Carlo sampling or particle filtering has shown to be powerful for nonlinear state estimation problems, thus holding a strong potential for executing the MPIC framework—this is also a focus of our study. Next, we will develop a new particle filter/smooth that presents high computational performance to enable fast MPIC of NSS models.

V. IMPLICIT PARTICLE FILTERING & SMOOTHING FOR MPIC

Particle filtering traces its roots to Monte Carlo simulation. At its heart, the technique approximates the posterior probability distribution of a system's state using statistical samples, i.e., particles, and as the state evolves, it recursively updates the particles using the principle of sequential importance sampling. With the sampling-based nature, particle filtering has great power in approximating complex distributions and searching the state space to make accurate state estimation for highly nonlinear systems. Its capacity is naturally useful here, and we will leverage particle filtering as well as its sibling,

particle smoothing, to approximately implement MPIC in this study.

However, particle filtering and smoothing may incur non-trivial computational burden, because one often must use a great number of particles to adequately approximate the target distribution—otherwise, the filtering or smoothing will fail as a majority of the particles might have zero weights in a phenomenon known as particle degeneracy and impoverishment. In our prior study [56], we proposed an implicit particle filtering approach, which shows effectiveness in overcoming the issue. Here, we expand the work in [56] by developing implicit particle smoothing to ensure fast computation in the execution of the MPIC framework. For the sake of completeness, we will show a systematic derivation in this section. We will first explain implicit importance sampling and then based on the concept, illustrate how to perform particle filtering/smoothing as banks of Kalman filters/smoothers. Finally, we will present the corresponding implementation of MPIC.

A. Implicit Importance Sampling

Let us begin with introducing importance sampling, which is the basis for particle filtering/smoothing. The method is intended to solve a fundamental problem in Bayesian estimation, which is evaluating

$$\mathbb{E}[g(\mathbf{x}) | \mathbf{y}] = \int g(\mathbf{x}) p(\mathbf{x} | \mathbf{y}) d\mathbf{x}, \quad (16)$$

where \mathbf{x} is a random vector, \mathbf{y} is the evidence or observation of \mathbf{x} , $g(\cdot)$ is an arbitrary function, and \mathbb{E} is the expectation operator. Here, we slightly abuse the notation without causing confusion. The target distribution $p(\mathbf{x} | \mathbf{y})$ is too complex to defy sampling in many cases. So instead we pick an easy-to-sample probability distribution $q(\mathbf{x})$, called the importance distribution, to draw particles $\{\mathbf{x}^i, i = 1, 2, \dots, N\}$. Using the particles, we can obtain an empirical approximation of (16) by

$$\mathbb{E}[g(\mathbf{x}) | \mathbf{y}] \approx \sum_{i=1}^N w^i g(\mathbf{x}^i), \quad w^i \propto \frac{1}{N} \frac{p(\mathbf{x}^i | \mathbf{y})}{q(\mathbf{x}^i)}, \quad (17)$$

where w^i is the so-called importance weight. This technique is known as importance sampling. Despite its utility, low approximation accuracy will result if most of the particles fall into the low-probability regions of $p(\mathbf{x} | \mathbf{y})$. The effects would carry over to particle filtering to underlie the aforementioned issue of particle degeneracy. Consequently, one must use a large, sometimes gigantic, number of particles to achieve satisfactory accuracy, at the expense of computational time.

Implicit importance sampling is motivated to remedy the situation. It aims to draw particles such that they lie in the high-probability regions of $p(\mathbf{x} | \mathbf{y})$ —when highly probable particles can be found, one can use fewer of them to achieve not only better approximation accuracy, but also lower computational costs. We introduce a reference probability distribution $p(\boldsymbol{\xi})$, where the random vector $\boldsymbol{\xi}$ has the same dimension as \mathbf{x} . Note that $p(\boldsymbol{\xi})$ must be amenable to sampling and have well-defined high-probability regions. We now seek to align the high-probability region of $p(\mathbf{x} | \mathbf{y})$ with that of $p(\boldsymbol{\xi})$. To this

end, we define $F(\mathbf{x}) = -\log p(\mathbf{x} | \mathbf{y})$ and $\varphi(\boldsymbol{\xi}) = -\log p(\boldsymbol{\xi})$, and let

$$F(\mathbf{x}) - \min F(\mathbf{x}) = \varphi(\boldsymbol{\xi}) - \min \varphi(\boldsymbol{\xi}). \quad (18)$$

Here, $\min F(\mathbf{x})$ and $\min \varphi(\boldsymbol{\xi})$ correspond to the highest-probability points of $p(\mathbf{x} | \mathbf{y})$ and $p(\boldsymbol{\xi})$, respectively. Suppose that a one-to-one mapping $\mathbf{x} = \Gamma(\boldsymbol{\xi})$ solves the algebraic equation (18). Then, we can use the mapping to get the particles $\mathbf{x}^i = \Gamma(\boldsymbol{\xi}^i)$, where \mathbf{x}^i is highly probable if $\boldsymbol{\xi}^i$ is taken from the highly probable region of $p(\boldsymbol{\xi})$. As shown in [56], the importance weight of \mathbf{x}^i is

$$w^i \propto \left| \frac{d\Gamma(\boldsymbol{\xi}^i)}{d\boldsymbol{\xi}^i} \right| \cdot \exp [-\min F(\mathbf{x}) + \min \varphi(\boldsymbol{\xi})].$$

Using the particles along with their weights, we can evaluate $\mathbb{E}[g(\mathbf{x}) | \mathbf{y}]$ along similar lines in (17). The evaluation will be more accurate because the particles are highly probable.

A computational bottleneck for implicit importance sampling is solving (18), especially when $F(\mathbf{x})$ is a nonlinear, nonconvex function. However, (18) will admit a closed-form, easy-to-compute expression of $\Gamma(\boldsymbol{\xi})$ in the Gaussian case. Specifically, if $\boldsymbol{\xi} \sim \mathcal{N}(\mathbf{0}, \mathbf{I})$ and

$$\begin{bmatrix} \mathbf{x} \\ \mathbf{y} \end{bmatrix} \sim \mathcal{N} \left(\begin{bmatrix} \mathbf{m}^x \\ \mathbf{m}^y \end{bmatrix}, \begin{bmatrix} \mathbf{P}^x & \mathbf{P}^{xy} \\ (\mathbf{P}^{xy})^\top & \mathbf{P}^y \end{bmatrix} \right),$$

then $p(\mathbf{x} | \mathbf{y}) \sim \mathcal{N}(\tilde{\mathbf{m}}, \tilde{\mathbf{P}})$, where

$$\begin{aligned} \tilde{\mathbf{m}} &= \mathbf{m}^x + \mathbf{P}^{xy} (\mathbf{P}^y)^{-1} (\mathbf{y} - \mathbf{m}^y), \\ \tilde{\mathbf{P}} &= \mathbf{P}^x - \mathbf{P}^{xy} (\mathbf{P}^y)^{-1} (\mathbf{P}^{xy})^\top, \\ \Gamma(\boldsymbol{\xi}) &= \tilde{\mathbf{m}} + \sqrt{\tilde{\mathbf{P}}} \boldsymbol{\xi}. \end{aligned}$$

Based on the explicit form of $\Gamma(\boldsymbol{\xi})$, we can create the particles \mathbf{x}^i and determine their importance weights w^i as

$$\mathbf{x}^i = \tilde{\mathbf{m}} + \sqrt{\tilde{\mathbf{P}}} \boldsymbol{\xi}^i, \quad w^i = \frac{1}{N},$$

where $\boldsymbol{\xi}^i$ for $i = 1, \dots, N$ are drawn from the high-probability region of $\mathcal{N}(\mathbf{0}, \mathbf{I})$. Then, (16) can be evaluated as

$$\mathbb{E}[g(\mathbf{x}) | \mathbf{y}] \approx \frac{1}{N} \sum_{i=1}^N g(\mathbf{x}^i).$$

In this case, implicit importance sampling is computationally fast to execute due to the expedient particle generation. The result is much useful as it will allow us to implement implicit particle filtering/smoothing later as banks of nonlinear Kalman filters/smoothers to achieve considerable computational efficiency.

B. Implicit Particle Filtering via a Bank of Kalman Filters

Given the system in (12), we consider the forward Bayesian filtering principle in (14), which implies

$$p(\bar{\mathbf{x}}_t | \bar{\mathbf{y}}_{k:t}) \propto p(\bar{\mathbf{y}}_t | \bar{\mathbf{x}}_t) p(\bar{\mathbf{x}}_t | \bar{\mathbf{x}}_{t-1}) p(\bar{\mathbf{x}}_{t-1} | \bar{\mathbf{y}}_{k:t-1}). \quad (19)$$

At time $t-1$, suppose that we have obtained the particles and their importance weights $\{\bar{x}_{t-1}^{f,i}, w_{t-1}^{f,i}, i = 1, \dots, N\}$ to form an empirical distribution that approximates $p(\bar{x}_{t-1} | \bar{y}_{k:t-1})$:

$$p(\bar{x}_{t-1} | \bar{y}_{k:t-1}) \approx \sum_{i=1}^N w_{t-1}^{f,i} \delta(\bar{x}_{t-1} - \bar{x}_{t-1}^{f,i}).$$

Here, f in the superscripts refers to filtering. The key question then is how to identify the particles $\bar{x}_t^{f,i}$ at time t using (19) and ensure that $\bar{x}_t^{f,i}$ will lie in the high-probability region of $p(\bar{x}_t | \bar{y}_{k:t})$. The implicit importance sampling principle tells us that we can draw highly probable particles of a reference random vector ξ_t and then map them to \bar{x}_t . Following (18), the mapping, denoted as $\Gamma^f : \xi_t \rightarrow \bar{x}_t$, can be made to solve

$$F_i^f(\bar{x}_t) - \min F_i^f(\bar{x}_t) = \varphi(\xi_t) - \min \varphi(\xi_t), \quad (20)$$

where $F_i^f(\bar{x}_t) = -\log p(\bar{x}_t | \bar{y}_{k:t})$, and $\varphi(\xi_t) = -\log p(\xi_t)$.

It is useful to have an explicitly expressed $\Gamma^f(\xi_t)$ to bypass the tedious computation to solve (20). This is usually impossible but can be achieved in the Gaussian case, as hinted in Section V-A. Our pursuit of the idea goes as below. Because

$$p(\bar{y}_t | \bar{x}_t, \bar{x}_{t-1}) = p(\bar{y}_t | \bar{x}_t),$$

it follows from (19) and Bayes' theorem that

$$p(\bar{x}_t | \bar{y}_{k:t}) \propto p(\bar{x}_t | \bar{y}_t, \bar{x}_{t-1}) p(\bar{y}_t | \bar{x}_{t-1}), \quad (21)$$

Let us approximate $p(\bar{x}_t | \bar{y}_{k:t})$ by a Gaussian distribution locally around $\bar{x}_{t-1}^{f,i}$:

$$\begin{bmatrix} \bar{x}_t \\ \bar{y}_t \end{bmatrix} \mid \bar{x}_{t-1} \sim \mathcal{N} \left(\begin{bmatrix} \mathbf{m}_t^{f,i} \\ \hat{y}_t^i \end{bmatrix}, \begin{bmatrix} \mathbf{P}_t^{x,f,i} & \mathbf{P}_t^{xy,f,i} \\ (\mathbf{P}_t^{xy,f,i})^\top & \mathbf{P}_t^{y,f,i} \end{bmatrix} \right),$$

where it is assumed that $\mathbf{m}_t^{f,i}$, $\mathbf{P}_t^{x,f,i}$, \hat{y}_t^i , $\mathbf{P}_t^{y,f,i}$, and $\mathbf{P}_t^{xy,f,i}$ can be constructed from $\bar{x}_{t-1}^{f,i}$. It then follows that

$$\bar{x}_t | \bar{y}_t, \bar{x}_{t-1} \sim \mathcal{N} \left(\tilde{\mathbf{m}}_t^{f,i}, \tilde{\mathbf{P}}_t^{x,f,i} \right), \quad (22)$$

where

$$\tilde{\mathbf{m}}_t^{f,i} = \mathbf{m}_t^{f,i} + \mathbf{K}_t^{f,i} (\bar{y}_t - \hat{y}_t^i), \quad (23a)$$

$$\tilde{\mathbf{P}}_t^{x,f,i} = \mathbf{P}_t^{x,f,i} - \mathbf{K}_t^{f,i} \mathbf{P}_t^{y,f,i} (\mathbf{K}_t^{f,i})^\top, \quad (23b)$$

$$\mathbf{K}_t^{f,i} = \mathbf{P}_t^{xy,f,i} (\mathbf{P}_t^{y,f,i})^{-1}. \quad (23c)$$

From (21)-(22), a local approximation for $p(\bar{x}_t | \bar{y}_{k:t})$ would emerge as $p(\bar{x}_t | \bar{y}_{k:t}) \propto \mathcal{N}(\tilde{\mathbf{m}}_t^{f,i}, \tilde{\mathbf{P}}_t^{x,f,i})$. If further letting $\xi_t \sim \mathcal{N}(\mathbf{0}, \mathbf{I})$, an explicit mapping will arise to solve (20), which is

$$\bar{x}_t = \Gamma^f(\xi_t) = \tilde{\mathbf{m}}_t^{f,i} + \sqrt{\tilde{\mathbf{P}}_t^{x,f,i}} \xi_t, \quad (24)$$

whereby one can draw a highly probable particle ξ_t^i from $p(\xi_t)$ and then compute $\bar{x}_t^{f,i}$.

As $\bar{x}_t = \Gamma^f(\xi_t)$ is one-on-one, the importance weight of \bar{x}_t^i is given by

$$w_t^{f,i} \propto w_{t-1}^{f,i} \cdot \left| \frac{d\Gamma^f(\xi_t^i)}{d\xi_t^i} \right| \cdot \exp \left[-\min F_i^f(\bar{x}_t^{f,i}) + \min \varphi(\xi_t) \right]$$

This, along with (21), leads to the normalized importance weight of $\bar{x}_t^{f,i}$ computed by

$$w_t^{f,i} = \frac{w_{t-1}^{f,i} p(\bar{y}_t | \bar{x}_t^{f,i})}{\sum_{j=1}^N w_{t-1}^{f,j} p(\bar{y}_t | \bar{x}_t^{f,j})}, \quad \bar{y}_t | \bar{x}_t^{f,j} \sim \mathcal{N} \left(\hat{y}_t^j, \tilde{\mathbf{P}}_t^{x,f,i} \right). \quad (25)$$

As $\bar{x}_t^{f,i}$ is considered as drawn from $p(\bar{x}_t | \bar{y}_{k:t})$, it has an associated covariance $\Sigma_t^{f,i}$ that is equal to $\tilde{\mathbf{P}}_t^{x,f,i}$, i.e.,

$$\Sigma_t^{f,i} = \tilde{\mathbf{P}}_t^{x,f,i}. \quad (26)$$

In the above, what draws our attention is that (23a)-(23c) is identical to the well-known Kalman update formulae. This indicates that the particle update can be done here by a nonlinear Kalman filter, and going further, one can use a bank of N nonlinear Kalman filters running in parallel to implement implicit particle filtering. In this implementation, every particle $\bar{x}_{t-1}^{f,i}$ is propagated forward by a Kalman filter, first to $\mathbf{m}_t^{f,i}$ by prediction (time-update) and then to $\tilde{\mathbf{m}}_t^{f,i}$ by update (measurement-update) as in (23); then, $\tilde{\mathbf{m}}_t^{f,i}$ will transform to $\bar{x}_t^{f,i}$ with the addition of ξ_t^i . The implementation, referred to as Kalman-IPF, is summarized in Algorithm 2, in which we use `KalmanPredict` and `KalmanUpdate` to represent the prediction-update procedure that is characteristic of Kalman filtering. The Kalman-IPF algorithm will not only inherit the merit of implicit particle filtering in using fewer but higher-quality particles to attain more accurate estimation, but also accelerate the search and determination of such particles. This makes it capable of offering both high accuracy and fast computation.

Remark 2: As aforementioned at the beginning of this section, particle filtering is beset by the issue of particle degeneracy. A commonly used remedy is resampling, which redraws particles based on the discrete empirical distribution formed by the current set of particles to decrease the presence of those particles with low weights. The Kalman-IPF algorithm is much less vulnerable to the issue due to its capability of finding out highly probable particles. However, we still recommend to include resampling in case particle degeneracy appears.

C. Implicit Particle Smoothing via a Bank of Kalman Smoothers

Now, we attempt to build implicit particle smoothing upon the notion of implicit importance sampling. We start with the backward Bayesian smoothing principle in (15) and approximate $p(\bar{x}_{t+1} | \bar{y}_{k:k+H})$ by the empirical distribution of the particles $\{\bar{x}_{t+1}^{s,i}, w_{t+1}^{s,i}, i = 1, \dots, N\}$, where the superscript s refers to smoothing. By (15), when a particle moves from $\bar{x}_{t+1}^{s,i}$ to $\bar{x}_t^{s,i}$, we only need to consider

$$p(\bar{x}_t | \bar{y}_{k:k+H}) \propto p(\bar{x}_t | \bar{x}_{t+1}, \bar{y}_{k:t}) p(\bar{x}_{t+1} | \bar{y}_{k:k+H}). \quad (27)$$

Since $\bar{x}_t^{s,i}$ is desired to fall into the high-probability regions of $p(\bar{x}_t | \bar{y}_{k:k+H})$, we want to find a mapping $\Gamma^s : \xi_t \rightarrow \bar{x}_t$, to project highly probable values of a reference vector ξ_t to

Algorithm 2 The Kalman-IPF Algorithm

- 1: Initialize the particles $\bar{x}_k^{f,i}$ for $i = 1, \dots, N$ with $\Sigma_k^{f,i}$ and $w_k^{f,i}$
- 2: **for** $t = k+1, k+2, \dots, k+H$ **do**
- 3: **for** $i = 1, 2, \dots, N$ **do**
- 4: Run Kalman filtering prediction
- 5: $\left[\mathbf{m}_t^{f,i}, \mathbf{P}_t^{\mathbf{x},f,i}, \hat{\mathbf{y}}_t^i, \mathbf{P}_t^{\mathbf{y},f,i}, \mathbf{P}_t^{\mathbf{x}\mathbf{y},f,i} \right] = \text{KalmanPredict} \left(\bar{x}_{t-1}^{f,i}, \Sigma_{t-1}^{f,i} \right)$
- 6: Run Kalman filtering update via (23)
- 7: $\left[\tilde{\mathbf{m}}_t^{f,i}, \tilde{\mathbf{P}}_t^{\mathbf{x},f,i} \right] = \text{KalmanUpdate} \left(\mathbf{m}_t^{f,i}, \mathbf{P}_t^{\mathbf{x},f,i}, \hat{\mathbf{y}}_t^i, \mathbf{P}_t^{\mathbf{y},f,i}, \mathbf{P}_t^{\mathbf{x}\mathbf{y},f,i} \right)$
- 8: Compute $\bar{x}_t^{f,i}$, $\Sigma_t^{f,i}$, and $w_t^{f,i}$ via (24)-(26)
- 9: **end for**
- 10: Do resampling if necessary
- 11: Output the filtered state estimate
- 12: **end for**

highly probable values of $\bar{x}_t^{s,i}$. Based on implicit importance sampling, we let

$$F_i^s(\bar{x}_t) - \min F_i^s(\bar{x}_t) = \varphi(\xi_t) - \min \varphi(\xi_t), \quad (28)$$

where $F_i^s(\bar{x}_t) = -\log p(\bar{x}_t | \bar{y}_{k:k+H})$, and $\varphi(\xi_t)$ follows the same definition in (20). As before, an explicit expression for $\bar{x}_t = \Gamma^s(\xi_t)$ will be sought after to solve (28). To achieve this, we impose the following local Gaussian approximations:

$$\begin{aligned} \left[\begin{array}{c} \bar{x}_t \\ \bar{x}_{t+1} \end{array} \right] \mid \bar{y}_{k:t} &\sim \mathcal{N} \left(\begin{bmatrix} \bar{x}_t^{f,i} \\ \mathbf{m}_{t+1}^{f,i} \end{bmatrix}, \begin{bmatrix} \Sigma_t^{f,i} & \mathbf{P}_{t,t+1}^{\mathbf{x},f,i} \\ \left(\mathbf{P}_{t,t+1}^{\mathbf{x},f,i} \right)^\top & \mathbf{P}_{t+1}^{\mathbf{x},f,i} \end{bmatrix} \right), \\ \bar{x}_{t+1} \mid \bar{y}_{k:k+H} &\sim \mathcal{N} \left(\bar{x}_{t+1}^{s,i}, \Sigma_{t+1}^{s,i} \right). \end{aligned}$$

Inserting the above Gaussian distributions into (27), we have

$$\bar{x}_t \mid \bar{y}_{k:k+H} \sim \mathcal{N} \left(\tilde{\mathbf{m}}_t^{s,i}, \tilde{\mathbf{P}}_t^{\mathbf{x},s,i} \right), \quad (29)$$

where

$$\tilde{\mathbf{m}}_t^{s,i} = \bar{x}_t^{f,i} + \mathbf{K}_t^{s,i} \left(\bar{x}_{t+1}^{s,i} - \mathbf{m}_{t+1}^{f,i} \right), \quad (30a)$$

$$\tilde{\mathbf{P}}_t^{\mathbf{x},s,i} = \Sigma_t^{f,i} + \mathbf{K}_t^{s,i} \left(\Sigma_{t+1}^{s,i} - \mathbf{P}_{t+1}^{\mathbf{x},f,i} \right) \left(\mathbf{K}_t^{s,i} \right)^\top, \quad (30b)$$

$$\mathbf{K}_t^{s,i} = \mathbf{P}_{t,t+1}^{\mathbf{x},f,i} \left(\mathbf{P}_{t+1}^{\mathbf{x},f,i} \right)^{-1}. \quad (30c)$$

Then, combining (29) with (28) readily gives

$$\bar{x}_t = \Gamma^s(\xi_t) = \tilde{\mathbf{m}}_t^{s,i} + \sqrt{\tilde{\mathbf{P}}_t^{\mathbf{x},s,i}} \xi_t, \quad (31)$$

when $\xi_t \sim \mathcal{N}(\mathbf{0}, \mathbf{I})$. Drawing a highly probable particle ξ_t^i , we can quickly compute $\bar{x}_t^{s,i}$ using (31) and obtain the associated covariance as

$$\Sigma_t^{s,i} = \tilde{\mathbf{P}}_t^{\mathbf{x},s,i}. \quad (32)$$

For backward smoothing, the importance weight of $\bar{x}_t^{s,i}$ is

$$w_t^{s,i} \propto \left| \frac{d\Gamma^s(\xi_t^i)}{d\xi_t^i} \right| \cdot \exp \left[-\min F_i^s \left(\bar{x}_t^{s,i} \right) + \min \varphi(\xi_t) \right],$$

which suggests that $w_t^{s,i} = w_t^{s,j}$ for any i and j due to (31). Hence, the normalized weight is

$$w_t^{s,i} = \frac{1}{N}. \quad (33)$$

The equal weights here indicate that all the particles have the same importance. Hence, the backward smoothing pass is free from the particle degeneracy issue, making it unnecessary to do resampling in this pass.

The backward update in (29)-(30) is identical to the Rauch-Tung-Striebel (RTS) Kalman smoothing. This inspires us to use a bank of nonlinear Kalman smoothers to implement implicit particle smoothing, with the smoothers running concurrently to update the individual particles. We summarize the implementation in Algorithm 3 and call it Kalman-IPS. In the algorithm, RTSKalmanSmooth represents the RTS backward update.

D. MPIC Based on Unscented Kalman-IPF and Kalman-IPS

We have shown that implicit particle filtering/smoothing can be approximately realized as banks of nonlinear Kalman filters/smoothers. Their exact implementation will depend on which Kalman filter to use. The literature provides a range of options, which, among others, include the extended, unscented, ensemble, and cubature Kalman filters. While all these filters have found their way into different applications, we note that the unscented Kalman filter is particularly suitable to enable MPIC for motion planning. First, the unscented Kalman filter offers second-order accuracy in estimation, which compares with the first-order accuracy of the extended Kalman filter. Second, it requires only moderate computation for low-dimensional nonlinear systems, and the considered NSS vehicle model falls into this case. Finally, its derivative-free computation eliminates a need for model linearization, which would have been burdensome for the NSS model.

Lying at the core of the unscented Kalman filter is the so-called unscented transform or \mathcal{UT} , which tracks the statistics in nonlinear transformations of Gaussian random vectors.

Algorithm 3 The Kalman-IPS Algorithm

- 1: Obtain the particles $\bar{x}_{k+H}^{s,i}$ for $i = 1, \dots, N$ with $\Sigma_{k+H}^{s,i}$ and $w_{k+H}^{s,i}$ from executing the Kalman-IPF algorithm
- 2: **for** $t = k + H, k + H - 1, \dots, k$ **do**
- 3: **for** $i = 1, 2, \dots, N$ **do**
- 4: Run Kalman smoothing update via (30)
- 5: $[\tilde{m}_t^{s,i}, \tilde{P}_t^{s,i}] = \text{RTSKalmanSmooth}(\bar{x}_{t+1}^{s,i}, \Sigma_{t+1}^{s,i}, \bar{x}_t^{f,i}, \Sigma_t^{f,i}, m_{t+1}^{f,i}, P_{t+1}^{x,f,i}, P_{t+1}^{x,f,i})$
- 6: **end for**
- 7: Output the state estimate
- 8: **end for**

Algorithm 4 The Unscented Transform (\mathcal{UT})

- 1: **Inputs:** $\mathbf{y} = \gamma(\mathbf{x}) + \mathbf{w}$, \mathbf{m}^x , \mathbf{P}^x , \mathbf{Q}
- 2: Generate the sigma points

$$\begin{aligned} \mathbf{x}^0 &= \mathbf{m}^x \\ \mathbf{x}^i &= \mathbf{m}^x + \sqrt{\alpha} \left[\sqrt{\mathbf{P}^x} \right]_i, \quad i = 1, 2, \dots, n \\ \mathbf{x}^{i+n} &= \mathbf{m}^x - \sqrt{\alpha} \left[\sqrt{\mathbf{P}^x} \right]_i, \quad i = 1, 2, \dots, n \end{aligned}$$
- 3: Pass the sigma points through $\gamma(\cdot)$

$$\mathbf{y}^i = \gamma(\mathbf{x}^i), \quad i = 0, 1, \dots, 2n$$
- 4: Compute \mathbf{m}^y , \mathbf{P}^y , and \mathbf{P}^{xy}

$$\begin{aligned} \mathbf{m}^y &= \sum_{i=0}^{2n} W_m^i \mathbf{y}^i \\ \mathbf{P}^y &= \sum_{i=0}^{2n} W_c^i (\mathbf{y}^i - \mathbf{m}^y) (\mathbf{y}^i - \mathbf{m}^y)^\top + \mathbf{Q} \\ \mathbf{P}^{xy} &= \sum_{i=0}^{2n} W_c^i (\mathbf{x}^i - \mathbf{m}^x) (\mathbf{y}^i - \mathbf{m}^y)^\top \end{aligned}$$
- 5: **Output:** \mathbf{m}^y , \mathbf{P}^y , \mathbf{P}^{xy}

*See [57] for the definitions of α , W_m^i , and W_c^i .

Briefly, consider $\mathbf{y} = \gamma(\mathbf{x}) + \mathbf{w}$, where \mathbf{x} and \mathbf{y} are random vectors, \mathbf{w} is a random noise vector, and $\gamma(\cdot)$ is an arbitrary nonlinear function. If we suppose $\mathbf{x} \sim \mathcal{N}(\mathbf{m}^x, \mathbf{P}^x)$ and $\mathbf{w} \sim \mathcal{N}(\mathbf{0}, \mathbf{Q})$, \mathcal{UT} will generate the statistics and form a Gaussian approximation for \mathbf{y} :

$$\begin{aligned} [\mathbf{m}^y, \mathbf{P}^y, \mathbf{P}^{xy}] &= \mathcal{UT}(\gamma, \mathbf{m}^x, \mathbf{P}^x, \mathbf{Q}), \\ \mathbf{y} &\sim \mathcal{N}(\mathbf{m}^y, \mathbf{P}^y). \end{aligned}$$

What \mathcal{UT} does behind this is identifying a set of sigma points (deterministically chosen particles) to approximately represent $p(\mathbf{x})$, projecting them through $\gamma(\cdot)$, and then using the transformed sigma points to compute \mathbf{m}^y , \mathbf{P}^y and \mathbf{P}^{xy} . A more detailed description is offered in Algorithm 4.

Here, we can apply \mathcal{UT} to the Kalman-IPF algorithm to perform KalmanPredict and KalmanUpdate. Subsequent to the forward filtering pass, the Kalman-IPS algorithm

can be run. Going forward with the idea, we can use the two algorithms to execute the MPIC framework for motion planning. The resultant MPIC implementation, called MPIC-X, is summarized in Algorithm 5.

VI. DISCUSSION

We devote this section to discuss the merits, implementation aspects, and potential extensions for the MPIC-X algorithm and the MPIC framework.

While arising out of the notion of MPC, the MPIC-X algorithm breaks away from mainstream MPC realizations based on gradient optimization. The primary difference is that it builds upon the perspective of Bayesian estimation and harnesses the power of Monte Carlo sampling to infer the best control decisions. This characteristic will yield high computational efficiency in handling control of NSS models for several reasons. First, the algorithm is derivative-free and thus obviates the need for generating and evaluating gradients. Second, the algorithm leverages the Markovianity of the system to perform recursive estimation for filtering and smoothing. This sequential computation deals with small-sized problems one after another to offer better overall efficiency. Finally, the Kalman-IPF and Kalman-IPS algorithms, which together serve as the computational engine of the MPIC-X algorithm, are capable of identifying much fewer but better-quality particles to accelerate search in the state and control space.

Some tricks will facilitate the implementation of the MPIC-X algorithm. First, we highlight that effective inferential control would require to set up a Bayesian estimation problem for (12) such that \bar{y}_t contains enough information about \bar{x}_t . This connects to the notions of observability and detectability for nonlinear systems. As per our experience, it often helps if we have some reference values in \bar{y}_t for all the unknown quantities in \bar{x}_t , or imposing meaningful limits for these quantities if there exist any. Second, we also find it useful in many cases to inflate the covariances \bar{Q} and \bar{R} with the same ratio. The covariance inflation makes no change to the original MPC formulation, but will enlarge the space in which to sample the particles. The consequent wider searches across the state and control space will improve the inferential control performance. Third, warm-start will expedite the success in

Algorithm 5 The MPIC-X Algorithm

1: Formulate the MPC problem in (8)
 2: Set up the virtual system in (9)
 3: **for** $k = 1, 2, \dots$ **do**
 // Forward filtering by Kalman-IPF
 4: Initialize the filtering particles $\bar{x}_k^{f,i}$ for $i = 1, \dots, N$ with $\Sigma_k^{f,i}$ and $w_k^{f,i}$
 5: **for** $t = k, k+1, \dots, k+H$ **do**
 6: **for** $i = 1, 2, \dots, N$ **do**
 7: Run KalmanPredict by $\mathcal{U}\mathcal{T}$

$$\begin{bmatrix} \mathbf{m}_t^{f,i}, \mathbf{P}_t^{\mathbf{x},f,i}, \mathbf{P}_{t-1,t}^{\mathbf{x},f,i} \end{bmatrix} = \mathcal{U}\mathcal{T} \left(\bar{\mathbf{f}}, \bar{\mathbf{x}}_{t-1}^{f,i}, \Sigma_{t-1}^{f,i}, \bar{\mathbf{Q}} \right)$$

$$\begin{bmatrix} \hat{\mathbf{y}}_t^i, \mathbf{P}_t^{\mathbf{y},f,i}, \mathbf{P}_t^{\mathbf{x}\mathbf{y},f,i} \end{bmatrix} = \mathcal{U}\mathcal{T} \left(\bar{\mathbf{h}}, \mathbf{m}_t^{f,i}, \mathbf{P}_t^{\mathbf{x},f,i}, \bar{\mathbf{R}} \right)$$
 8: Run KalmanUpdate

$$\tilde{\mathbf{m}}_t^{f,i} = \mathbf{m}_t^{f,i} + \mathbf{K}_t^{f,i} (\bar{\mathbf{y}}_t - \hat{\mathbf{y}}_t^i),$$

$$\tilde{\mathbf{P}}_t^{\mathbf{x},f,i} = \mathbf{P}_t^{f,i} - \mathbf{K}_t^{f,i} \mathbf{P}_t^{\mathbf{y},f,i} (\mathbf{K}_t^{f,i})^\top$$

$$\mathbf{K}_t^{f,i} = \mathbf{P}_t^{\mathbf{x}\mathbf{y},f,i} (\mathbf{P}_t^{\mathbf{y},f,i})^{-1}$$
 9: Draw a highly probable particle $\xi_t^i \sim \mathcal{N}(\mathbf{0}, \mathbf{I})$, and update the filtering particle

$$\bar{\mathbf{x}}_t^{f,i} = \tilde{\mathbf{m}}_t^{f,i} + \sqrt{\tilde{\mathbf{P}}_t^{\mathbf{x},f,i}} \xi_t^i, \quad \Sigma_t^{f,i} = \tilde{\mathbf{P}}_t^{\mathbf{x},f,i}$$

$$w_t^{f,i} = \frac{w_{t-1}^{f,i} p(\bar{\mathbf{y}}_t | \bar{\mathbf{x}}_{t-1}^{f,i})}{\sum_{j=1}^N w_{t-1}^{f,j} p(\bar{\mathbf{y}}_t | \bar{\mathbf{x}}_{t-1}^{f,j})}, \quad \bar{\mathbf{y}}_t | \bar{\mathbf{x}}_{t-1}^{f,i} \sim \mathcal{N} \left(\hat{\mathbf{y}}_t^i, \mathbf{P}_t^{\mathbf{y},f,i} \right)$$
 10: **end for**
 11: Do resampling if necessary
 12: **end for**
 // Backward smoothing by Kalman-IPS
 13: Initialize the smoothing particles by $\bar{\mathbf{x}}_{k+H}^{s,i} = \bar{\mathbf{x}}_{k+H}^{f,i}$ and $\Sigma_{k+H}^{s,i} = \Sigma_{k+H}^{f,i}$ for $i = 1, \dots, N$
 14: **for** $t = k+H-1, k+H-2, \dots, k$ **do**
 15: **for** $i = 1, 2, \dots, N$ **do**
 16: Run RTSKalmanUpdate

$$\tilde{\mathbf{m}}_t^{s,i} = \bar{\mathbf{x}}_t^{f,i} + \mathbf{K}_t^{s,i} (\bar{\mathbf{x}}_{t+1}^{s,i} - \mathbf{m}_{t+1}^{f,i})$$

$$\tilde{\mathbf{P}}_t^{\mathbf{x},s,i} = \Sigma_t^{f,i} + \mathbf{K}_t^{s,i} (\Sigma_{t+1}^{s,i} - \mathbf{P}_{t+1}^{\mathbf{x},f,i}) (\mathbf{K}_t^{s,i})^\top$$

$$\mathbf{K}_t^{s,i} = \mathbf{P}_{t,t+1}^{\mathbf{x},f,i} (\mathbf{P}_{t+1}^{\mathbf{x},f,i})^{-1}$$
 17: Draw a highly probable particle $\xi_t^i \sim \mathcal{N}(\mathbf{0}, \mathbf{I})$, and update the smoothing particle

$$\bar{\mathbf{x}}_t^{s,i} = \tilde{\mathbf{m}}_t^{s,i} + \sqrt{\tilde{\mathbf{P}}_t^{\mathbf{x},s,i}} \xi_t^i, \quad \Sigma_t^{s,i} = \tilde{\mathbf{P}}_t^{\mathbf{x},s,i}, \quad w_t^{s,i} = \frac{1}{N}$$
 18: **end for**
 19: **end for**
 20: Compute the final estimate for $\bar{\mathbf{x}}_{k:k+H}$

$$\hat{\mathbf{x}}_k^* = \frac{1}{N} \sum_{i=1}^N \bar{\mathbf{x}}_k^{s,i}$$
 21: Export and apply control decisions
 22: **end for**

the filtering/smoothing pass of the MPIC-X algorithm. As a simple yet effective way, one can use $\bar{x}_{k+1}^{s,i}$ for $i = 1, \dots, N$ obtained at time k to initialize the filtering particles for the subsequent horizon starting at time $k + 1$. A final trick is to replace the ideal barrier function in (10) with a modified softplus function

$$\psi(x) = \frac{1}{a} \ln(1 + e^{bx}),$$

where $a, b > 0$ are tunable parameters. By tuning a and b , one can change the shape of $\psi(x)$ to adjust the constraint satisfaction level.

Various extensions are available to expand the MPIC framework. First, if the original MPC problem has a non-quadratic control objective $J(\bar{x}_{k:k+H}) = \sum_{t=k}^{k+H} \ell(\bar{x}_t)$, where $\ell(\cdot)$ is an arbitrary nonlinear function, we can follow [36] to introduce a binary random variable $O_t \in \{0, 1\}$ in place of \bar{y}_t in (12) such that

$$p(O_t = 1 | \bar{x}_t) \propto \exp(-\ell(\bar{x}_t)).$$

Here, O_t measures the probability that the virtual system in (12) behaves optimally. Skipping the proof, we conclude that the corresponding MPIC problem will ask for Bayesian estimation to determine $p(\bar{x}_{k:k+H} | O_{k:k+H} = 1)$. Second, the MPIC-X framework can be implemented by more filtering/smoothing methods that provide some desirable properties. For instance, we can leverage ensemble Kalman filtering/smoothing to enable MPIC of high-dimensional nonlinear or NSS systems as they have superior computational advantages for such systems. Finally, while the MPIC framework is motivated by the motion planning problem, it lends itself well to a broader spectrum of control applications, especially those that can be dealt with by MPC.

VII. NUMERICAL SIMULATIONS

In this section, we conduct a simulation study that applies the MPIC-X algorithm to motion planning in autonomous highway driving. The simulation deals with the cases of overtaking, emergency braking, and on-ramp merging. In what follows, we first describe the simulation setting, then examine the overtaking scenario with a comprehensive comparison against gradient-based MPC, and finally show the emergency braking and ramp merging scenarios.

A. The Simulation Setting

We use the MATLAB Autonomous Driving Toolbox running on a workstation with a 3.5GHz Intel Core i9-10920X CPU and 128GB of RAM to set up and implement the driving scenarios. The EV can access all the necessary road information and localize itself using equipped sensors. It acquires driving references from a higher-level route planner that include waypoints and desired speeds, among others. The EV is also capable of predicting the future positions of the OVs over the upcoming planning horizon. The OV's trajectories are pre-specified using the Toolbox. In the simulation, the sampling period is $\Delta t = 0.1$ s, and the EV is set to maintain a safe distance of 1 m for simplicity. We consider

different horizon lengths for H and particle numbers for N when implementing the MPIC-X algorithm in the overtaking scenario for the purpose of comparison. We let $H = 40$ and $N = 10$ in the emerging braking and ramp merging scenarios.

An objective in the simulation of the overtaking scenario is to evaluate the capabilities of the MPIC-X algorithm and gradient-based MPC in handling NSS models with different structures. To this end, we consider the following feedforward neural network structures:

- Net-1: a single hidden layer with 512 neurons;
- Net-2: two hidden layers with 128 neurons in each layer;
- Net-3: four hidden layers with 64, 128, 128, and 64 neurons in each layer.

The activation function for all the hidden layers is the tanh function. For convenience, we use the single-track bicycle model to generate synthetic training datasets and then train Nets 1 – 3 using the Adam optimizer. Only Net-2 is used in the emergency braking and ramp merging scenarios.

B. The Overtaking Scenario

In this scenario, the EV and OVs are running on a curved, two-lane highway road. As shown in Fig. 3, the EV (in red) is initially behind two OVs (in green and blue), moving at slower speeds. To overtake the OVs, the EV computes motion plans using the MPIC-X algorithm and then maneuvers. The MPIC-X algorithm adopts Net-2 for the NSS model, uses $N = 10$ particles, and the planning horizon is $H = 40$. Fig. 3 shows that the EV successfully overtakes the OVs without collision despite the curvature of the road. Fig. 4 further shows the actuation profiles in accelerating and steering and the profiles of the distance between the EV and OVs. As is seen, the EV manages to comply with the driving and safety constraints throughout the maneuvering process. The results show that the MPIC-X algorithm effectively identifies motion plans to accomplish the overtaking task.

Proceeding forward, we compare the MPIC-X algorithm against gradient-based MPC in terms of computation time and planning performance. The gradient-based MPC uses the default interior-point method in MATLAB to solve the constrained optimization problem. For a fair comparison, the analytical form of the gradient is pre-computed offline and then called in during online optimization, and the optimization is also warm-started to accelerate the search. To achieve a comprehensive assessment, we perform the simulation for different planning horizons by letting $H = 10, 20, 40$, and 60 , and for the MPIC-X algorithm, use different particle numbers, $N = 10, 30, 50$, and 80 . Each setting comes with ten simulation runs to find out the average computational time.

Table I summarizes the numerical results and comparison following extensive simulations. The overarching observations are as follows.

- The gradient-based MPC requires hefty computation. The computation time will increase significantly when the planning horizon H grows from 10 to 40, and the gradient-based MPC even fails to find optima when $H = 60$. The neural network architecture, especially the number of layers, plays another crucial role in the

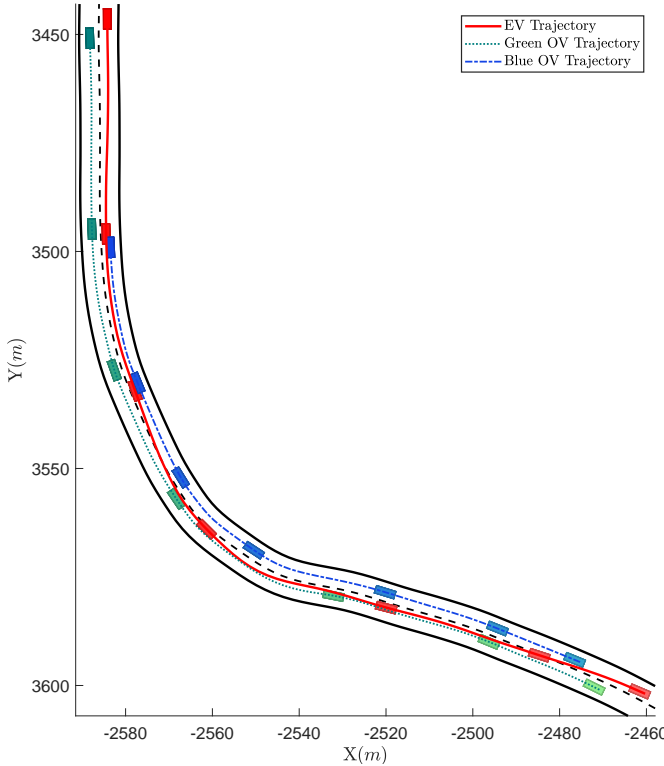


Fig. 3: Trajectories of the EV (in red) and OVs (in green and blue) in the overtaking scenario. The color change from light to dark indicates the passage of the driving time.

computation. If we compare the time consumed in the cases of Nets-1/2 and Net-3 — the more hidden layers, the more nonlinear the NSS model. These results reflect the limitations and struggle of the gradient-based MPC in control of NSS models.

- The MPIC-X algorithm, however, shows a strong capability in handling NSS models. In contrast to the gradient-based MPC, it reduces computation time by remarkably large margins—at least by 95% in all settings. Even though its computation time also increases with the planning horizon H , the increase rates are much milder. Unlike the gradient-based MPC, the MPIC-X algorithm can still deliver reasonable and satisfactory performance even when $H = 60$. It is interesting and important to note that the MPIC-X algorithm has almost indistinguishable computational speeds for Nets-1/2/3, due to the power of sampling in dealing with nonlinearity. Its computational insensitivity to the neural network architecture will be a notable merit in controlling NSS models. It is unsurprising that the computation time of the MPIC-X algorithm depends on the number of particles used in implementing the MPIC-X algorithm, but the increase rates are no more than linear. Also, the cost performance is worth examining. When the planning horizon is 10 or 20, the MPIC-X algorithm shows slightly higher, but still comparable, costs to the gradient-based MPC. However, it leads to better performance by a substantial degree when the planning horizon expands to 40 or 60 to yield

more complicated optimization problems. Finally, it is noteworthy to mention that the MPIC-X algorithm with just $N = 10$ particles can deliver good enough cost performance and outstanding computational efficiency.

Fig. 5 illustrates the computation time of the MPIC-X algorithm and gradient-based MPC versus the planning horizon lengths, and Fig. 6 further offers a heatmap-based depiction. The comparison in both points to the outstanding computational efficiency and scalability of the MPIC-X algorithm. Fig. 7 demonstrates the cost performance over time. What it shows is consistent with what is described above—the MPIC-X algorithm presents comparable performance when the planning horizon is $H = 10$ or 20, and fares much better when $H = 40$ and 60.

C. The Braking and On-ramp Merging Scenarios

A leading cause of traffic accidents on highway roads is the build-up of traffic congestion. In this circumstance, the EV must be able to decelerate from a high speed and when the OVs in front of it come to a complete stop, brake to zero speed, while considering passenger comfort and avoiding collision. We simulate the scenario by applying the MPIC-X algorithm with $N = 10$ particles and utilizing the Net-2 for the vehicle model.

Fig. 8 depicts the trajectories of the EV and OVs. Initially, the OVs travel faster than the EV and then the green OV rapidly decelerate to a complete stop. During the first three seconds, the higher-level route planner is assumed to be unaware of the upcoming congestion, keeping the reference speed unaltered. Despite this, the EV starts to decelerate as well, as seen in Fig. 9b. Meanwhile, the EV slightly deviates from the lane center in search of a feasible trajectory that can maintain the reference speed, as seen in Fig. 8. However, no such trajectory exists as the OVs occupy both lanes, so the EV decides to stay in its current lane and brake to avoid a collision. This behavior demonstrates the effectiveness of MPIC's constraint awareness to ensure collision-free planning while adhering to all driving constraints, as shown in Fig. 9.

On-ramp merging is another common scenario for autonomous highway driving. However, it is challenging because an autonomous vehicle often finds it difficult to determine the right moment and right speed to safely merge into the traffic. Here, we assume light traffic to make the problem amenable enough to center the focus on the evaluation of the MPIC-X algorithm. As in the braking scenario, the MPIC-X algorithm uses $N = 10$ particles and the Net-2-based vehicle model.

As shown in Fig. 10, the EV opts to merge at the third second. It first slows down to a safe speed in the initial stage of the scenario, as shown in Fig. 11a. Then, the EV increases the steering angle to enter into the traffic, as shown in Fig. 11b. In the maneuvering process, the EV gets close to the green OV but manages to keep a safe distance, as is seen in Fig. 11c. After merging onto the highway, it moves behind the OV in green without collision avoidance.

The above simulation results show that the MPIC-X algorithm and the MPIC framework are effective at finding motion plans for autonomous vehicles and enabling control

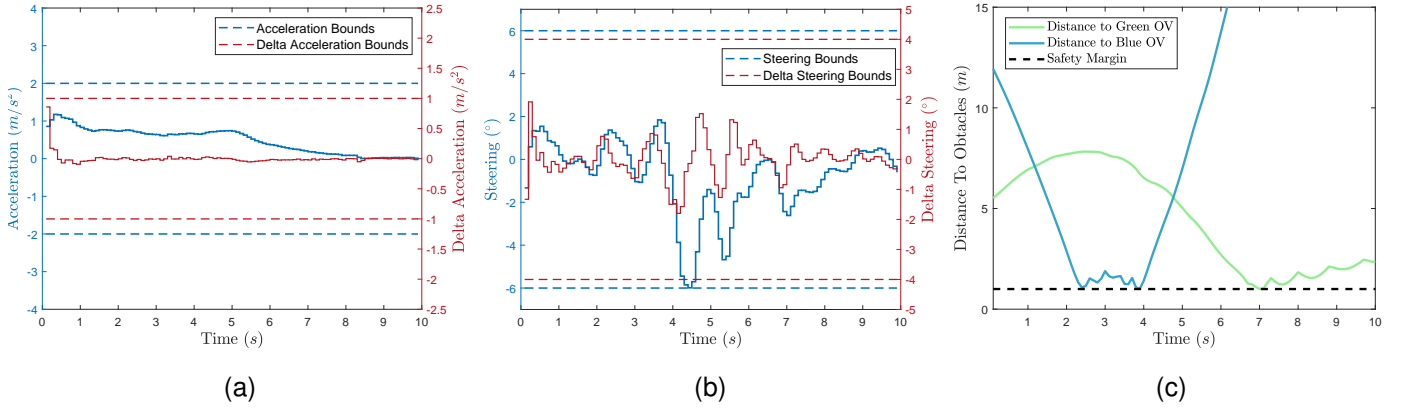


Fig. 4: Simulation results for the overtaking scenario: (a) the acceleration and incremental acceleration profiles in solid curves, with respective bounds in dashed lines; (b) the steering and incremental steering profiles in solid lines, with their respective bounds in dashed lines. (c) distance between the EV and OVs, with the dashed-line safe margin.

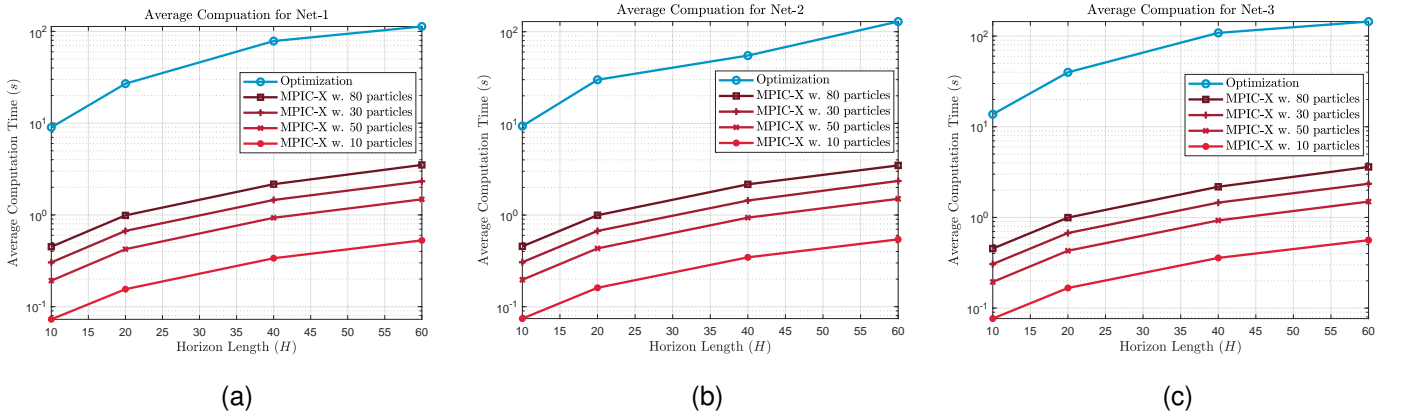


Fig. 5: Computational time comparison between MPIC-X algorithm and gradient-based MPC for different networks, horizon lengths, and particle numbers: (a) Net-1; (b) Net-2; (c) Net-3.

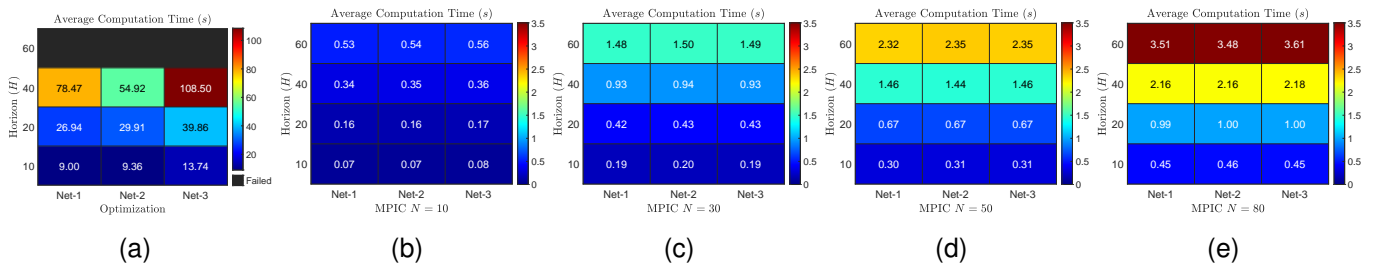


Fig. 6: Computation time comparison in the heatmap format: (a) the gradient-based MPC; (b) MPIC-X with $N = 10$ particles; (c) MPIC-X with $N = 30$ particles; (d) MPIC-X with $N = 50$ particles; (e) MPIC-X with $N = 80$ particles. The color bars differ for the plots.

of NSS models. Given the results, we highlight again that: 1) the MPIC-X algorithm offers high computational efficiency in solving MPC of NSS models, 2) its computational performance is almost insensitive to neural network architectures, 3) it can achieve good enough cost performance with just a few particles, and 4) the algorithm can achieve success in solving large-scale MPC problems where gradient-based optimization may easily fail.

VIII. CONCLUSION

The rise of autonomous driving presents ever-growing demands for better motion planning technologies. MPC has proven to be a useful approach for this application. Meanwhile, machine learning has found its way into vehicle modeling due to its capacity of accurately capturing vehicle dynamics. However, despite the potential for improving motion planning design, machine learning models have been unyielding to

TABLE I: Numerical comparison of MPIC-X and optimization

| Network | Horizon (H) | Method | Total Cost | Average Computation Time (s) | Relative Cost Change (%) | Relative Computation Time Change (%) |
|--------------------------|--------------------|------------------------|------------|------------------------------|--------------------------|--------------------------------------|
| Net-1 (512) | 10 | Optimization | 11,919 | 9.00 | — | — |
| | | MPIC-X w. 10 particles | 13,041 | 0.073 | 9.42 | -99.19 |
| | | MPIC-X w. 30 particles | 12,888 | 0.192 | 8.13 | -97.86 |
| | | MPIC-X w. 50 particles | 12,880 | 0.304 | 8.06 | -96.63 |
| | | MPIC-X w. 80 particles | 12,611 | 0.450 | 5.81 | -95.00 |
| | 20 | Optimization | 11,910 | 26.94 | — | — |
| | | MPIC-X w. 10 particles | 12,615 | 0.155 | 5.92 | -99.42 |
| | | MPIC-X w. 30 particles | 12,494 | 0.423 | 4.90 | -98.43 |
| | | MPIC-X w. 50 particles | 12,339 | 0.669 | 3.61 | -97.52 |
| | | MPIC-X w. 80 particles | 12,307 | 0.989 | 3.34 | -96.33 |
| | 40 | Optimization | 29,261 | 78.47 | — | — |
| | | MPIC-X w. 10 particles | 12,514 | 0.337 | -57.23 | -99.57 |
| | | MPIC-X w. 30 particles | 12,362 | 0.930 | -57.75 | -98.82 |
| | | MPIC-X w. 50 particles | 12,336 | 1.455 | -57.84 | -98.15 |
| | | MPIC-X w. 80 particles | 12,324 | 2.162 | -57.88 | -97.25 |
| | 60 | Optimization | — | — | — | — |
| | | MPIC-X w. 10 particles | 12,357 | 0.528 | — | — |
| | | MPIC-X w. 30 particles | 12,332 | 1.478 | — | — |
| | | MPIC-X w. 50 particles | 12,345 | 2.325 | — | — |
| | | MPIC-X w. 80 particles | 12,263 | 3.505 | — | — |
| Net-2 (128–128) | 10 | Optimization | 12,159 | 9.36 | — | — |
| | | MPIC-X w. 10 particles | 13,345 | 0.071 | 9.76 | -99.19 |
| | | MPIC-X w. 30 particles | 13,292 | 0.197 | 9.32 | -97.86 |
| | | MPIC-X w. 50 particles | 13,171 | 0.306 | 8.33 | -96.63 |
| | | MPIC-X w. 80 particles | 13,055 | 0.455 | 7.37 | -95.00 |
| | 20 | Optimization | 12,050 | 29.92 | — | — |
| | | MPIC-X w. 10 particles | 13,066 | 0.161 | 8.44 | -99.42 |
| | | MPIC-X w. 30 particles | 12,938 | 0.432 | 7.37 | -98.43 |
| | | MPIC-X w. 50 particles | 12,821 | 0.671 | 6.40 | -97.52 |
| | | MPIC-X w. 80 particles | 12,176 | 0.995 | 1.05 | -96.33 |
| | 40 | Optimization | 14,680 | 54.92 | — | — |
| | | MPIC-X w. 10 particles | 12,937 | 0.345 | -11.87 | -99.57 |
| | | MPIC-X w. 30 particles | 12,820 | 0.936 | -12.67 | -98.82 |
| | | MPIC-X w. 50 particles | 12,619 | 1.44 | -14.04 | -98.15 |
| | | MPIC-X w. 80 particles | 12,545 | 2.163 | -14.55 | -97.25 |
| | 60 | Optimization | — | — | — | — |
| | | MPIC-X w. 10 particles | 12,426 | 0.543 | — | — |
| | | MPIC-X w. 30 particles | 12,858 | 1.503 | — | — |
| | | MPIC-X w. 50 particles | 12,755 | 2.354 | — | — |
| | | MPIC-X w. 80 particles | 12,315 | 3.476 | — | — |
| Net-3 (64–128–128–64) | 10 | Optimization | 12,077 | 13.74 | — | — |
| | | MPIC-X w. 10 particles | 12,903 | 0.077 | 6.84 | -99.42 |
| | | MPIC-X w. 30 particles | 12,842 | 0.194 | 6.34 | -98.58 |
| | | MPIC-X w. 50 particles | 12,863 | 0.306 | 6.51 | -97.77 |
| | | MPIC-X w. 80 particles | 12,715 | 0.453 | 5.28 | -96.70 |
| | 20 | Optimization | 11,684 | 39.86 | — | — |
| | | MPIC-X w. 10 particles | 12,201 | 0.167 | 4.42 | -99.58 |
| | | MPIC-X w. 30 particles | 12,463 | 0.429 | 6.66 | -98.92 |
| | | MPIC-X w. 50 particles | 12,439 | 0.673 | 6.45 | -98.31 |
| | | MPIC-X w. 80 particles | 12,469 | 0.996 | 6.72 | -97.50 |
| | 40 | Optimization | 14,889 | 108.5 | — | — |
| | | MPIC-X w. 10 particles | 12,570 | 0.358 | -15.57 | -99.67 |
| | | MPIC-X w. 30 particles | 12,482 | 0.926 | -16.16 | -99.15 |
| | | MPIC-X w. 50 particles | 12,382 | 1.456 | -16.83 | -98.66 |
| | | MPIC-X w. 80 particles | 12,329 | 2.178 | -17.18 | -97.99 |
| | 60 | Optimization | — | — | — | — |
| | | MPIC-X w. 10 particles | 12,490 | 0.561 | — | — |
| | | MPIC-X w. 30 particles | 12,424 | 1.494 | — | — |
| | | MPIC-X w. 50 particles | 12,455 | 2.351 | — | — |
| | | MPIC-X w. 80 particles | 12,381 | 3.607 | — | — |

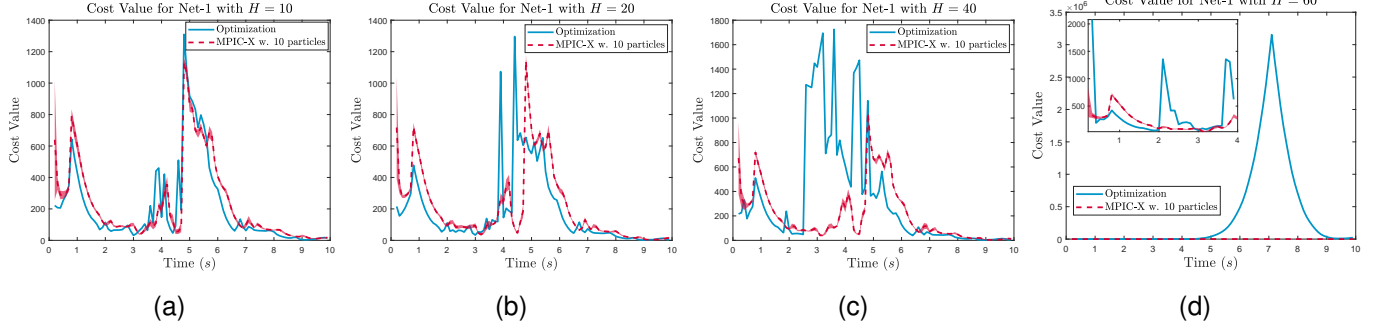


Fig. 7: Cost performance comparison between the MPIC-X algorithm with ten particles and the gradient-based MPC for Net-1 at different horizon lengths: (a) $H = 10$; (b) $H = 20$; (c) $H = 40$; (d) $H = 60$, where the gradient-based MPC fails.

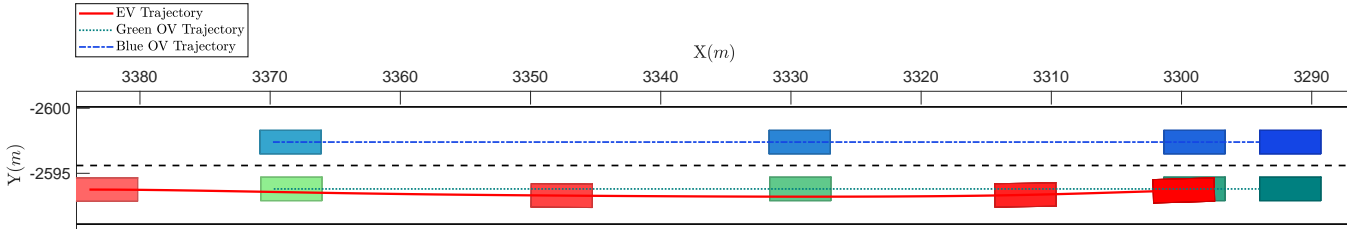


Fig. 8: Trajectories of the EV (in red) and OVs (in green and blue) in the braking scenario.

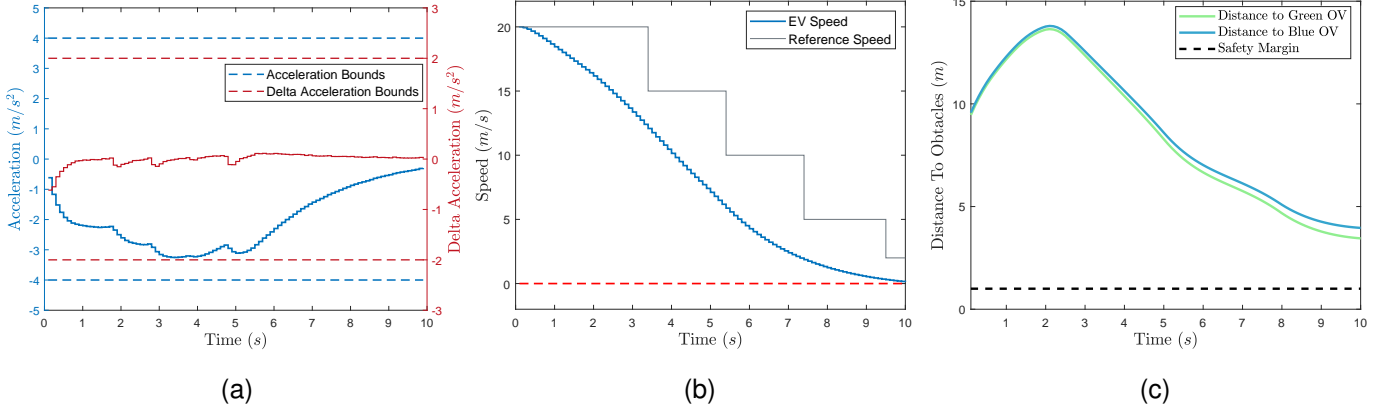


Fig. 9: Simulation results for the braking scenario: (a) the acceleration and incremental acceleration profiles in solid curves, with respective bounds in dashed lines; (b) the steering and incremental steering profiles in solid lines, with their respective bounds in dashed lines. (c) distance between the EV and OVs, with the dashed-line safe margin.

MPC, as their strong nonlinearity and nonconvexity resist gradient-based optimization.

In this paper, we consider the problem of MPC of NSS models and pursue a different perspective—inferring the best control decisions from the control objectives and constraints. The perspective, inspired by the classical control-estimation duality, opens up the avenue for executing MPC through Bayesian estimation and some powerful estimation techniques. Based on this notion, we first reformulate the MPC problem for motion planning into an equivalent Bayesian state smoothing problem. To tackle the problem, we consider particle filtering/smoothing, which, based on Monte Carlo sampling, can handle highly nonlinear systems. This technique, however, often requires large numbers of particles and thus heavy

computation to succeed. We then derive and propose implicit particle filtering/smoothing based on banks of unscented Kalman filters. This novel approach manages to use much fewer particles in estimation by sampling at highly probable regions of the target distribution to achieve high computational efficiency and accuracy. The resultant framework, called MPIC, and algorithm, called MPIC-X, thus arise out of the development.

We apply the MPIC-X algorithm to the highway overtaking, braking, and on-ramp merging scenarios via extensive simulations. The simulation results show that the MPIC-X algorithm is highly effective at dealing with the control of NSS models. Its computation is very fast and insensitive to neural network architectures and well applicable and scalable to long

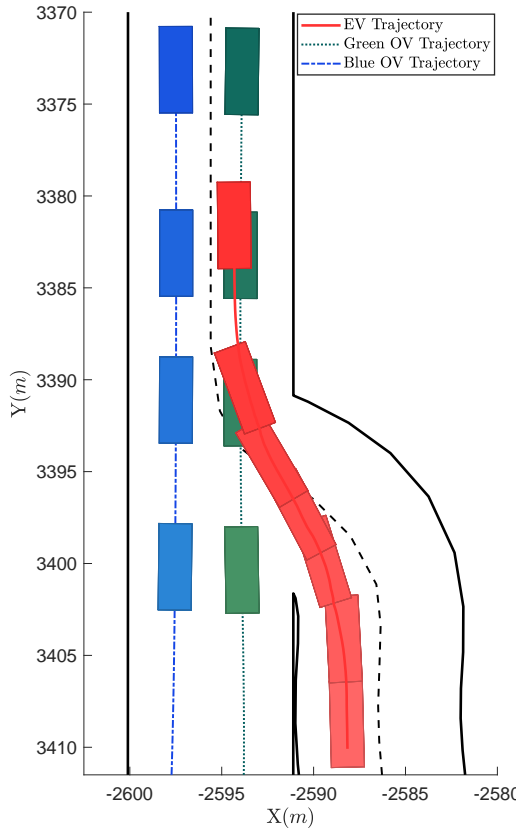


Fig. 10: Trajectories of the EV (in red) and OVs (in green and blue) in the on-ramp merging scenario.

prediction horizons, compared to gradient-based MPC. The proposed algorithm and framework can find prospective use in various other engineering problems that involve the control of machine learning models.

REFERENCES

- [1] S. A. Bagloee, M. Tavana, M. Asadi, and T. Oliver, "Autonomous vehicles: challenges, opportunities, and future implications for transportation policies," *Journal of Modern Transportation*, vol. 24, no. 4, pp. 284–303, 2016.
- [2] B. Paden, M. Cap, S. Z. Yong, D. Yershov, and E. Frazzoli, "A survey of motion planning and control techniques for self-driving urban vehicles," *IEEE Transactions on Intelligent Vehicles*, vol. 1, no. 1, pp. 33–55, 2016.
- [3] L. Claussmann, M. Revilloud, D. Gruyer, and S. Glaser, "A review of motion planning for highway autonomous driving," *IEEE Transactions on Intelligent Transportation Systems*, vol. 21, no. 5, pp. 1826–1848, 2020.
- [4] N. A. Spielberg, M. Brown, N. R. Kapania, J. C. Kegelman, and J. C. Gerdes, "Neural network vehicle models for high-performance automated driving," *Science Robotics*, vol. 4, no. 28, 2019.
- [5] L. Hewing, J. Kabzan, and M. N. Zeilinger, "Cautious model predictive control using Gaussian process regression," *IEEE Transactions on Control Systems Technology*, vol. 28, no. 6, pp. 2736–2743, 2020.
- [6] A. Nagabandi, G. Kahn, R. S. Fearing, and S. Levine, "Neural network dynamics for model-based deep reinforcement learning with model-free fine-tuning," in *Proceedings of the IEEE International Conference on Robotics and Automation*, 2018, pp. 7559–7566.
- [7] A. Doucet, N. Freitas, and N. Gordon, Eds., *Sequential Monte Carlo Methods in Practice*. New York, NY: Springer, 2001.
- [8] S. Särkkä, *Bayesian Filtering and Smoothing*, ser. Institute of Mathematical Statistics Textbooks, 2013.
- [9] A. J. Chorin and X. Tu, "Implicit sampling for particle filters," *Proceedings of the National Academy of Sciences*, vol. 106, no. 41, pp. 17 249–17 254, 2009.
- [10] A. Chorin, M. Morzfeld, and X. Tu, "Implicit particle filters for data assimilation," *Communications in Applied Mathematics and Computational Science*, vol. 5, no. 2, pp. 221 – 240, 2010.
- [11] S. M. LaValle, "Rapidly-exploring random trees : a new tool for path planning," *The annual research report*, 1998.
- [12] E. Frazzoli, M. A. Dahleh, and E. Feron, "Real-time motion planning for agile autonomous vehicles," *Journal of Guidance, Control, and Dynamics*, vol. 25, no. 1, pp. 116–129, 2002.
- [13] Y. Kuwata, J. Teo, G. Fiore, S. Karaman, E. Frazzoli, and J. P. How, "Real-time motion planning with applications to autonomous urban driving," *IEEE Transactions on Control Systems Technology*, vol. 17, no. 5, pp. 1105–1118, 2009.
- [14] S. Karaman and E. Frazzoli, "Sampling-based algorithms for optimal motion planning," *The International Journal of Robotics Research*, vol. 30, no. 7, pp. 846–894, 2011.
- [15] J. hwan Jeon, R. V. Cowagi, S. C. Peters, S. Karaman, E. Frazzoli, P. Tsotras, and K. Iagnemma, "Optimal motion planning with the half-car dynamical model for autonomous high-speed driving," in *Proceedings of American Control Conference*, 2013, pp. 188–193.
- [16] K. Berntorp, T. Hoang, and S. Di Cairano, "Motion planning of autonomous road vehicles by particle filtering," *IEEE Transactions on Intelligent Vehicles*, vol. 4, no. 2, pp. 197–210, 2019.
- [17] A. Rucco, G. Notarstefano, and J. Hauser, "Computing minimum lap-time trajectories for a single-track car with load transfer," in *2012 IEEE 51st IEEE Conference on Decision and Control (CDC)*, 2012, pp. 6321–6326.
- [18] C. Roessmann, W. Feiten, T. Woesch, F. Hoffmann, and T. Bertram, "Trajectory modification considering dynamic constraints of autonomous robots," in *Proceedings of the 7th German Conference on Robotics*, 2012, pp. 1–6.
- [19] M. Shomin and R. Hollis, "Fast, dynamic trajectory planning for a dynamically stable mobile robot," in *2014 IEEE/RSJ International Conference on Intelligent Robots and Systems*, 2014, pp. 3636–3641.
- [20] J. Funke, M. Brown, S. M. Erlien, and J. C. Gerdes, "Collision avoidance and stabilization for autonomous vehicles in emergency scenarios," *IEEE Transactions on Control Systems Technology*, vol. 25, no. 4, pp. 1204–1216, 2017.
- [21] J. Nilsson, P. Falcone, M. Ali, and J. Sjöberg, "Receding horizon maneuver generation for automated highway driving," *Control Engineering Practice*, vol. 41, pp. 124–133, 2015.
- [22] H. Guo, C. Shen, H. Zhang, H. Chen, and R. Jia, "Simultaneous trajectory planning and tracking using an MPC method for cyber-physical systems: A case study of obstacle avoidance for an intelligent vehicle," *IEEE Transactions on Industrial Informatics*, vol. 14, no. 9, pp. 4273–4283, 2018.
- [23] C. Liu, S. Lee, S. Varnhagen, and H. E. Tseng, "Path planning for autonomous vehicles using model predictive control," in *2017 IEEE Intelligent Vehicles Symposium (IV)*, 2017, pp. 174–179.
- [24] Y. S. Henglai Wei, "MPC-based motion planning and control enables smarter and safer autonomous marine vehicles: Perspectives and a tutorial survey," p. 8, 2023.
- [25] F. Eiras, M. Hawasly, S. V. Albrecht, and S. Ramamoorthy, "A two-stage optimization-based motion planner for safe urban driving," *IEEE Transactions on Robotics*, vol. 38, no. 2, pp. 822–834, 2022.
- [26] S. M. Thornton, S. Pan, S. M. Erlien, and J. C. Gerdes, "Incorporating ethical considerations into automated vehicle control," *IEEE Transactions on Intelligent Transportation Systems*, vol. 18, no. 6, pp. 1429–1439, 2017.
- [27] J. Chen, W. Zhan, and M. Tomizuka, "Autonomous driving motion planning with constrained iterative LQR," *IEEE Transactions on Intelligent Vehicles*, vol. 4, no. 2, pp. 244–254, 2019.
- [28] X. Qian, I. Navarro, A. de La Fortelle, and F. Moutarde, "Motion planning for urban autonomous driving using Bézier curves and MPC," in *Proceedings of the IEEE 19th International Conference on Intelligent Transportation Systems*, 2016, pp. 826–833.
- [29] R. E. Kalman, "A new approach to linear filtering and prediction problems," *Journal of Basic Engineering*, vol. 82, no. 1, pp. 35–45, 03 1960.
- [30] E. Todorov, "General duality between optimal control and estimation," in *2008 47th IEEE Conference on Decision and Control*, 2008, pp. 4286–4292.
- [31] ———, "Efficient computation of optimal actions," *Proceedings of the National Academy of Sciences*, vol. 106, no. 28, pp. 11 478–11 483, 2009.
- [32] J. W. Kim and P. G. Mehta, "Duality for nonlinear filtering II: optimal control," *IEEE Transactions on Automatic Control*, 2023, in press.

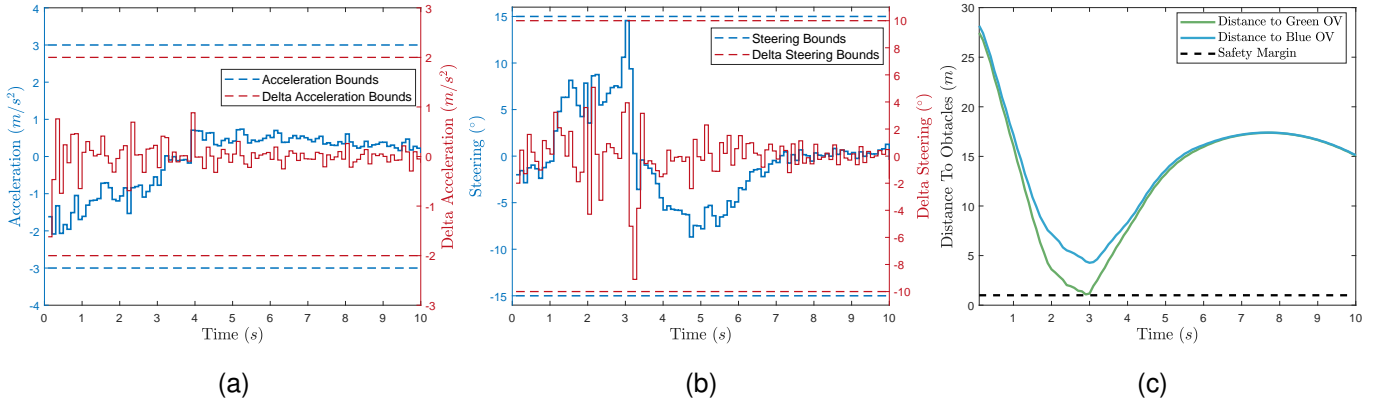


Fig. 11: Simulation results for the on-ramp scenario: (a) the acceleration and incremental acceleration profiles in solid curves, with respective bounds in dashed lines; (b) the steering and incremental steering profiles in solid lines, with their respective bounds in dashed lines. (c) distance between the EV and OVs, with the dashed-line safe margin.

- [33] H. J. Kappen, V. GÃ³mez, and M. Opper, "Optimal control as a graphical model inference problem," *Machine Learning*, vol. 87, no. 2, pp. 159–182, 2012.
- [34] G. Williams, P. Drews, B. Goldfain, J. M. Rehg, and E. A. Theodorou, "Information-theoretic model predictive control: Theory and applications to autonomous driving," *IEEE Transactions on Robotics*, vol. 34, no. 6, pp. 1603–1622, 2018.
- [35] S. P. Q. Syed and H. Bai, "Parameterized input inference for approximate stochastic optimal control," in *Proceedings of American Control Conference*, 2023, pp. 2574–2579.
- [36] M. Toussaint, "Robot trajectory optimization using approximate inference," in *Proceedings of the 26th Annual International Conference on Machine Learning*, 2009.
- [37] D. Stahl and J. Hauth, "PF-MPC: Particle filter-model predictive control," *Systems & Control Letters*, vol. 60, no. 8, pp. 632–643, 2011.
- [38] I. Askari, S. Zeng, and H. Fang, "Nonlinear model predictive control based on constraint-aware particle filtering/smoothing," in *2021 American Control Conference (ACC)*, 2021, pp. 3532–3537.
- [39] I. Askari, B. Badnava, T. Woodruff, S. Zeng, and H. Fang, "Sampling-based nonlinear MPC of neural network dynamics with application to autonomous vehicle motion planning," in *2022 American Control Conference (ACC)*, 2022, pp. 2084–2090.
- [40] U. Rosolia, X. Zhang, and F. Borrelli, "Data-driven predictive control for autonomous systems," *Annual Review of Control, Robotics, and Autonomous Systems*, vol. 1, no. 1, pp. 259–286, 2018.
- [41] L. Hewing, K. P. Wabersich, M. Menner, and M. N. Zeilinger, "Learning-based model predictive control: Toward safe learning in control," *Annual Review of Control, Robotics, and Autonomous Systems*, vol. 3, no. 1, pp. 269–296, 2020.
- [42] S. Piche, B. Sayyar-Rodsari, D. Johnson, and M. Gerules, "Nonlinear model predictive control using neural networks," *IEEE Control Systems Magazine*, vol. 20, no. 3, pp. 53–62, 2000.
- [43] M. Ławryńczuk, *MPC Algorithms Based on Neural State-Space Models*. Cham: Springer International Publishing, 2014, pp. 139–166.
- [44] T. Salzmann, E. Kaufmann, J. Arrizabalaga, M. Pavone, D. Scaramuzza, and M. Ryll, "Real-time neural MPC: Deep learning model predictive control for quadrotors and agile robotic platforms," *IEEE Robotics and Automation Letters*, vol. 8, no. 4, pp. 2397–2404, 2023.
- [45] A. Bemporad, "A piecewise linear regression and classification algorithm with application to learning and model predictive control of hybrid systems," *IEEE Transactions on Automatic Control*, vol. 68, no. 6, pp. 3194–3209, 2023.
- [46] J. Pohlodek, H. Alsmeier, B. Morabito, C. Schlauch, A. Savchenko, and R. Findeisen, "Stochastic model predictive control utilizing Bayesian neural networks," in *Proceedings of American Control Conference*, 2023, pp. 603–608.
- [47] F. Cursi, V. Modugno, L. Lanari, G. Oriolo, and P. Kormushev, "Bayesian neural network modeling and hierarchical MPC for a tendon-driven surgical robot with uncertainty minimization," *IEEE Robotics and Automation Letters*, vol. 6, no. 2, pp. 2642–2649, 2021.
- [48] F. Bünning, A. Schalbetter, A. Aboudonia, M. H. de Badyn, P. Heer, and J. Lygeros, "Input convex neural networks for building MPC," in *Proceedings of the 3rd Conference on Learning for Dynamics and Control*, ser. Proceedings of Machine Learning Research, vol. 144, 2021, pp. 251–262.
- [49] Y. Yang, K. Caluwaerts, A. Iscen, T. Zhang, J. Tan, and V. Sindhwani, "Data efficient reinforcement learning for legged robots," in *Proceedings of the Conference on Robot Learning*, ser. Proceedings of Machine Learning Research, vol. 100, 2020, pp. 1–10.
- [50] M. Maiworm, D. Limon, and R. Findeisen, "Online learning-based model predictive control with Gaussian process models and stability guarantees," *International Journal of Robust and Nonlinear Control*, vol. 31, no. 18, pp. 8785–8812, 2021.
- [51] C. J. Ostafew, A. P. Schoellig, and T. D. Barfoot, "Robust constrained learning-based NMPC enabling reliable mobile robot path tracking," *The International Journal of Robotics Research*, vol. 35, no. 13, pp. 1547–1563, 2016.
- [52] M. Forgiore, M. Mejari, and D. Piga, "Learning neural state-space models: do we need a state estimator?" *ArXiv preprint arXiv:2206.12928*, 2022.
- [53] X. Du, K. K. K. Htet, and K. K. Tan, "Development of a genetic-algorithm-based nonlinear model predictive control scheme on velocity and steering of autonomous vehicles," *IEEE Transactions on Industrial Electronics*, vol. 63, no. 11, pp. 6970–6977, 2016.
- [54] C. Rao, J. Rawlings, and D. Mayne, "Constrained state estimation for nonlinear discrete-time systems: stability and moving horizon approximations," *IEEE Transactions on Automatic Control*, vol. 48, no. 2, pp. 246–258, 2003.
- [55] *Foundations of Modern Probability*. Springer Cham, 2021.
- [56] I. Askari, M. A. Haile, X. Tu, and H. Fang, "Implicit particle filtering via a bank of nonlinear Kalman filters," *Automatica*, vol. 145, p. 110469, 2022.
- [57] H. Fang, N. Tian, Y. Wang, M. Zhou, and M. A. Haile, "Nonlinear bayesian estimation: from Kalman filtering to a broader horizon," *IEEE/CAA Journal of Automatica Sinica*, vol. 5, no. 2, pp. 401–417, 2018.